Delft University of Technology

Document Version
Final published version

Licence
CC BY

Citation (APA)
Beernink, S., Hartog, N., Vardon, P. J., & Bloemendal, M. (2026). How density and viscosity differences cause nonuniform flow distribution across well screens and impact heat recovery of HT-ATES systems. *Hydrogeology Journal*. https://doi.org/10.1007/s10040-026-03154-8

Important note
To cite this publication, please use the final published version (if applicable).
Please check the document version above.

Copyright
In case the licence states “Dutch Copyright Act (Article 25fa)”, this publication was made available Green Open Access via the TU Delft Institutional Repository pursuant to Dutch Copyright Act (Article 25fa, the Taverne amendment). This provision does not affect copyright ownership.
Unless copyright is transferred by contract or statute, it remains with the copyright holder.

Sharing and reuse
Other than for strictly personal use, it is not permitted to download, forward or distribute the text or part of it, without the consent of the author(s) and/or copyright holder(s), unless the work is under an open content license such as Creative Commons.

Takedown policy
Please contact us and provide details if you believe this document breaches copyrights.
We will remove access to the work immediately and investigate your claim.

This work is downloaded from Delft University of Technology.

Hydrogeology Journal
https://doi.org/10.1007/s10040-026-03154-8

PAPER

How density and viscosity differences cause nonuniform flow distribution across well screens and impact heat recovery of HT-ATES systems

Stijn Beernink[1,2] · Niels Hartog[1,3] · Philip J. Vardon[2] · Martin Bloemendal[2,4]

Received: 17 December 2025 / Accepted: 7 August 2026
© The Author(s) 2026

Abstract
It is well known that heat recovery of high-temperature aquifer thermal energy storage (HT-ATES) systems is negatively impacted by buoyancy-driven flow of the injected hot, low-density water during storage. Density differences, however, also affect pressure head conditions within the well and therefore pressure head differences with the aquifer. Thus, it was anticipated that nonuniform flow distribution across the well screen may occur even when homogeneous aquifer permeability is assumed. In this study, the extent and conditions under which nonuniform flow across HT-ATES well screens occurs, influenced by both variable density and viscosity, were evaluated using both numerical and analytical approaches. Results show that with larger density differences (injection temperatures up to 90 °C) and lower well pressure heads, flow distribution is increasingly nonuniform, with the highest flow rates across the top part of the well screen, up to multiple times the average flow rate. Nonuniformity is described analytically by the maximum depth of injection ($D_{\mathrm{inj,max}}$) and the maximum normalized flow at the top of the aquifer ($q_{\mathrm{n,max}}$). Decreasing viscosities with higher temperatures further amplify buoyancy-induced nonuniform flow distribution, with flow rates up to 3.7 times the average. Flow distribution is shown to be asymmetrical during injection and extraction, and besides contributing to losses, the extent to which flow distribution is nonuniform, consequently also results in substantially higher maximum velocities across the borehole wall, which is a critical design parameter to prevent clogging. A literature screening of HT-ATES storage conditions in practice highlights the relevance of considering buoyancy-induced nonuniform flow distribution.

Keywords Aquifer thermal energy storage (ATES) · Variable groundwater density and viscosity · Well hydraulics · Nonuniform flow distribution · Geothermal systems

Introduction

To increase the cost-efficiency and global use of renewable energy, large-scale thermal energy storage plays an important role in the energy transition by reducing the mismatch between energy availability and demand (Dobson et al. 2025; Henry et al. 2020). Aquifer thermal energy storage (ATES) systems are used to seasonally store large amounts of thermal energy in the subsurface at temperatures ranging from 5 to > 100 °C (Fleuchaus et al. 2018). This technique utilizes aquifers to store and recover thermal energy by injecting and extracting heated groundwater using tube wells. In general, this is done using the most common well type, a vertically screened well with an artificial filter pack (Houben 2015a). ATES at low storage temperatures (e.g. < 25 °C), typically used in conjunction with a heat pump for heating, is commonly used in different parts of the world and particularly in western Europe (Fleuchaus et al. 2018). At higher temperatures (50 to > 100 °C) HT-ATES shows great potential to seasonally store thermal energy at higher energy densities and for direct use in meeting heating demand, which can further reduce greenhouse gas (GHG) emissions (Bloemendal et al. 2020). However, implementation of HT-ATES in practice is

✉ Stijn Beernink
stijn.beernink@kwrwater.nl

1 KWR Water Research Institute, PO Box 1072, 3430 BB Nieuwegein, The Netherlands

2 Delft University of Technology, Delft, The Netherlands

3 Faculty of Geosciences, Utrecht University, Utrecht, The Netherlands

4 TNO Geological Survey of the Netherlands, Utrecht, The Netherlands

currently still relatively undeveloped, with only a handful of systems operational worldwide (Fleuchaus et al. 2020).

The technical and economic success of HT-ATES depends strongly on the recovery efficiency of thermal energy from its wells, i.e., the ratio between the recovered energy and the injected energy (Sommer et al. 2013). When excess thermal energy is available, groundwater is extracted from the aquifer through the well screen into one well of the HT-ATES doublet (warm well, Fig. 1a), the groundwater is heated at the surface via a heat exchanger and is injected into the other well of the doublet (hot well, Fig. 1a). During injection, the thermal front of the infiltrating hot water propagates into the aquifer, and heat losses occur at the thermal front and confining layers owing to conduction, dispersion and potentially buoyancy-driven flow (Beernink et al. 2024; Bloemendal and Hartog 2018; Buscheck et al. 1983; Doughty et al. 1982; Schout et al. 2014). During periods of heating demand, extraction occurs from the hot well, while groundwater is extracted from the aquifer through the well screen into the well bore up to the heat exchanger and the cooled water is

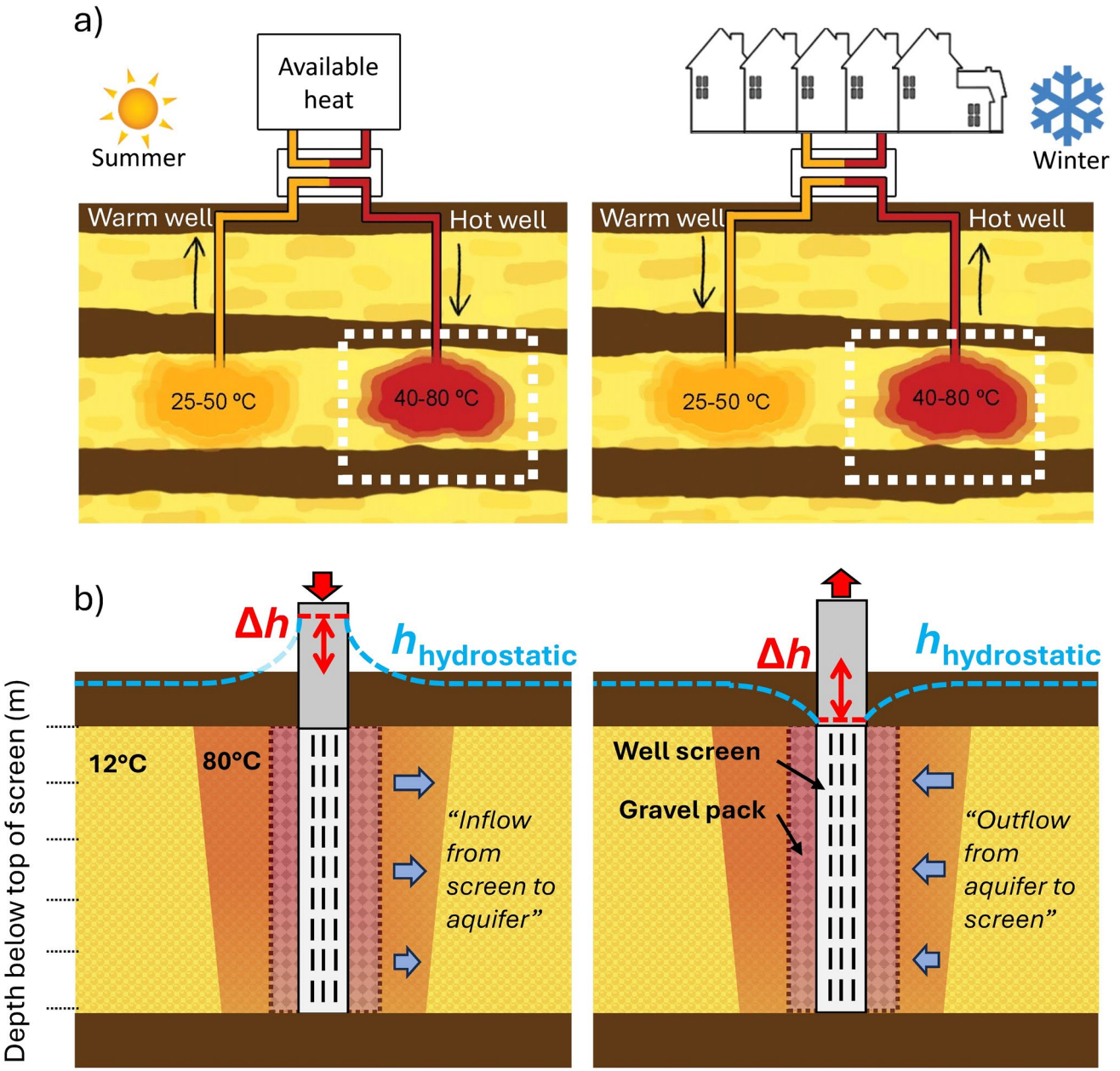

Fig. 1 **a** Schematic overview (not to scale) of the operation of a HT-ATES system during heat loading in summer (left, injection in the hot well) and unloading in winter (right, extraction from the hot well). **b** Close-up of the well screen of the hot well (not to scale) and the surrounding subsurface during injection (Δh pressure head increase in well) and extraction (Δh pressure head decrease in well)

injected into the other well. Thermal energy from the hot well is typically only produced as long as the temperature of the recovered groundwater is above a certain cut-off temperature limited by the specifications of the supplied energy system (Birdsell et al. 2021; Bloemendal et al. 2020).

The temperature of the recovered groundwater is determined by the heat flow distribution across the length of the well screen, which is determined by both the temperature and the flow rate of the water entering the well. Typically, the vertical temperature profile across the well screen is nonuniform during recovery owing to the buoyancy-driven tilting (e.g. Hellström et al. (1988)) that occurs because of density differences when water is stored at higher temperatures (typically up to ~90 °C). Buoyancy, however, also affects the pressure distribution within the well and its difference with the pressure in the surrounding aquifer that drives flow in or out of the storage aquifer. Combined with the temperature-dependent viscosity of water, these pressure differences may cause nonuniform flow during both injection and extraction across the well screen, even when assuming a homogeneous permeability in the storage aquifer, similar to the processes described in, e.g., CO_2 injection wells and (water) flooding of oil/gas reservoirs (Craig et al. 1957; Han et al. 2016; Taku Ide et al. 2007). Despite its potential impact on heat recovery, the conditions under which nonuniform flow across HT-ATES wells may occur have not been previously considered. Therefore, this study assessed the effects of variable water density and viscosity across a range of injection temperatures and varying operational and hydrogeological conditions on the flow distribution across HT-ATES well screens.

To this end, the behavior of the inflow and outflow across ATES well screens was studied for a set of representative operational and hydrogeological conditions. A series of different well models that include or exclude the influence of temperature-induced variable density and viscosity on the flow distribution across the well screen during injection and extraction were implemented and simulation results were compared and verified with theoretical and analytical approaches. This study aimed to provide clear insights to understand (1) how different factors affect the occurrence of buoyancy-induced nonuniform flow distribution across the well screen, (2) how varying storage conditions affect the degree of nonuniformity, and (3) how nonuniform flow distribution affects heat recovery and can be considered in the design of HT-ATES wells.

Materials and methods

Theory: ATES wells and pressure head conditions with variable density

ATES systems utilize aquifers to inject, store and extract heated groundwater. A doublet of vertical tube wells, similar to groundwater extraction wells, is generally used to do this (Fig. 1a). During ATES operation (Fig. 1b), the induced near-well hydraulic pressure head (Δh) conditions in the aquifer depend on the rates of injection and extraction. During injection, the pressure head in the well increases such that the needed inflow from the screen to the aquifer is obtained (Fig. 1b). Conversely, during extraction, the pressure head in the well is decreased, and outflow from the aquifer into the well occurs.

For flow in vertical tube wells, Houben (2015b) showed that only minor pressure head losses are expected owing to the resistance of the vertical flow in the well bore itself, ranging between 0.5–2% compared to the total expected head losses for relevant well operational conditions. Hence, the largest head loss components occur outside the well bore, i.e., because of flow in the gravel pack due not only to skin but mainly to the induced radial flow in the aquifer. Therefore, when water with a density (as a function of salinity and temperature) equal to that of the ambient groundwater in the storage aquifer is injected from the well, uniform inflow/outflow across the well screen is expected for homogeneous aquifer and gravel pack conditions. Hence, the injection pressure head (the positive Δh (m) compared to the hydrostatic aquifer) and the extraction pressure head (the negative Δh (m) compared to the hydrostatic aquifer) are, in this case, equal along the depth of the well screen. The pressure head difference Δh (m) needed in the well relative to the ambient hydrostatic pressure in the aquifer to inject/extract the water can be calculated using Thiem's equation for steady-state flow in a confined aquifer assuming fully horizontal and radially symmetric flow:

$$\Delta h_{\text{Thiem}} = \frac{Q}{2\pi K_{\text{h}} L} \ln\left(\frac{R}{r}\right) \tag{1}$$

where Q is the flow rate (m^3/day), K_{h} is the horizontal hydraulic conductivity (m/day), L the screen length/aquifer thickness (m), R the outer boundary radial distance (m), and r the well screen radius (m).

For situations where water density is variable, the pressure at a certain depth is determined by both the depth and the (average) density of the overlying water column. Hence, the pressure head difference per meter depth between two separated vertical water columns (columns x and y) is the result of the (average) density difference between the two fluids and the absolute reference density (Post et al. 2007) and can be expressed as:

$$\Delta \rho_{\text{r}} = \frac{(\rho_{\text{x}} - \rho_{\text{y}})}{\rho_{\text{x}}} \tag{2}$$

where $\Delta \rho_{\text{r}}$ (-) is the decrease in equivalent pressure head (m) per meter depth (m), and ρ_{x} and ρ_{y} are the water density (kg/m^3) of the two columns, respectively, with water in column x as the reference density. By multiplying this with the total

depth below a certain reference depth, the pressure head difference at depth D is calculated:

$$\Delta h_{\text{buoy}} = \Delta \rho_{\text{r}} \cdot D \tag{3}$$

where Δh_{buoy} is the buoyancy pressure head difference (m) owing to the density difference between the two columns, and D the depth in meters (or height of the water column). Hence, with increasing density difference and increasing depth, the buoyancy pressure difference also increases.

For HT-ATES specifically, hot water of lower density (ρ_{inj}) is injected into an aquifer with lower-temperature ambient groundwater of higher density (ρ_{amb}). Thus, additional pressure head (Δh_{inj}) is already required to push the relatively light hot water down into the well tube (Δh_{wt}, scenarios A and B in Fig. 2) until the top of screen and then further down into the screened well section (scenarios C–F in Fig. 2). For the latter, the pressure head difference with the aquifer results both in the downward flow of the hot water into the well tube and the radial flow of the hot water into the aquifer. As the depth below the surface level to the top of the well screen increases, and the density difference between the injected and average ambient groundwater density increases, the injection pressure head (Δh_{wt}) thus also increases. However, how much pressure head is needed to push the hot water column to the top of the well screen does not influence the pressure head difference with the aquifer, as infiltration from the well screen into the aquifer only occurs below the top of the well screen. Therefore, in this study, only the depth-independent pressure differences that occur down from the top of the well screen are considered. Below the top of the well screen, increasing pressure head (Δh_{inj}) (for a given density difference $\Delta\rho$) results in deeper maximum injection depth (D_{inj}) and larger flow rates (Fig. 2c–f). When the depth of injection reaches the bottom of the aquifer ($D_{\text{inj}} = L$, Fig. 2e, f), further increase of the injection pressure head Δh_{inj} only results in increasing flow into the aquifer. Hence, in this study, only the pressure head that occurs in the well screen Δh_{ws} is simulated and assessed from the top of the well screen downwards.

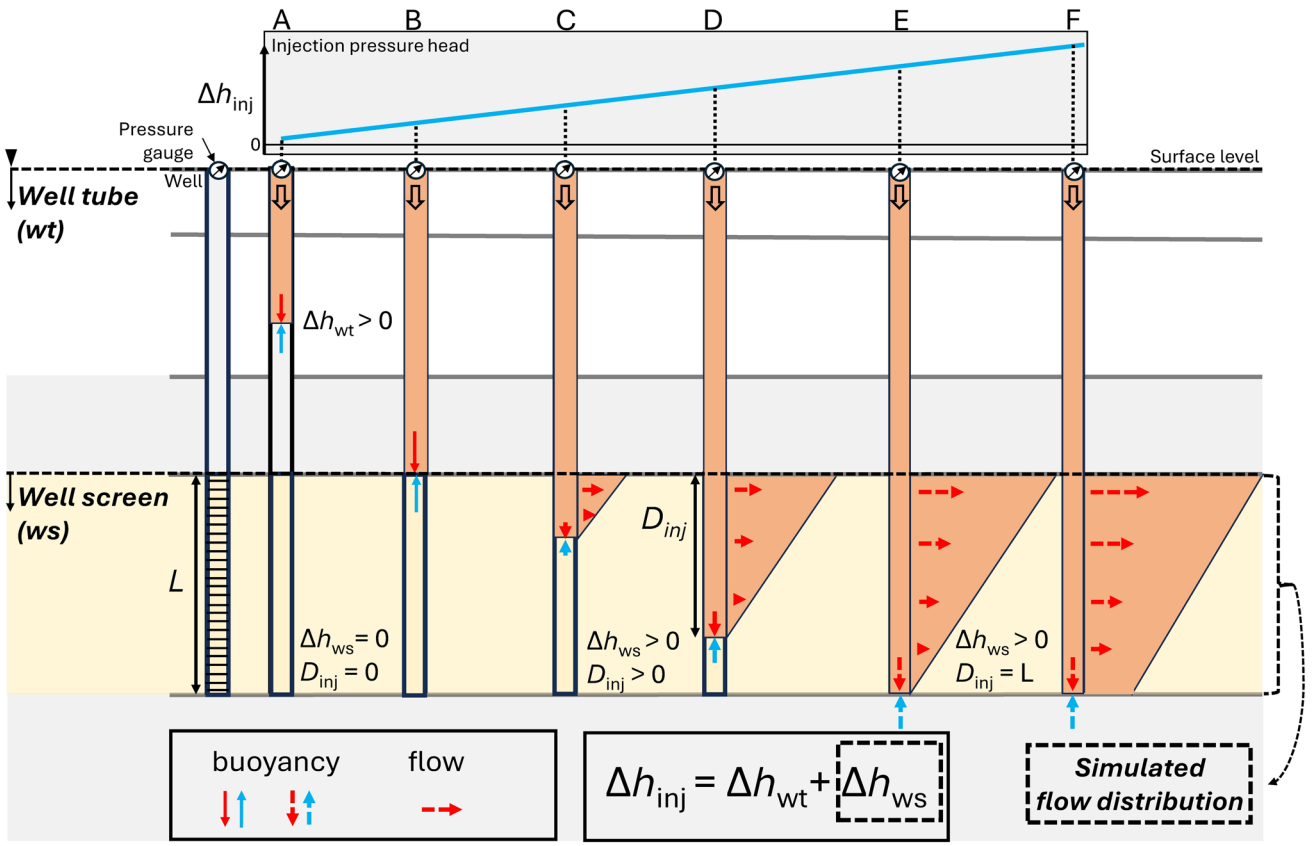

Fig. 2 Distribution of pressure head components at increasing pumping pressures (scenarios A–F) in a schematic subsurface layering example with screen placement and injection into the fourth layer. Scenarios A–B: low injection pressure head, the injection head results in equilibrium in the well bore but is not sufficient to have inflow across the well screen. Scenarios C–D: the injection pressure is sufficient to inject beyond the top of the well screen and inflow occurs from the well bore across the well screen; however, the bottom of the well is not reached ($D_{\text{inj}} < L$). Scenarios E–F: relatively large injection pressure head (higher flow rate) results in inflow across the entire length of the well screen ($D_{\text{inj}} = L$)

Thermo-hydraulic simulator

The numerical simulator SEAWATv4 was used to simulate the thermo-hydraulic behavior of the inflow/outflow across the well screen and the stored heat in the aquifer. SEAWATv4 is a finite difference model that incorporates the dependent flow of density and viscosity (Langevin et al. 2008), and is based on a combination of MODFLOW-2000 (Harbaugh et al. 2000), the flow component, and the MT3DMs transport model (Zheng and Wang 1999). MODFLOW is a numerical groundwater flow model based on Darcy's law. The SEAWATv4 model used in this study is operated from Python through the FloPy package (Bakker et al. 2016; Mindel et al. 2021). Because of radial symmetry, an axisymmetric modelling approach (Fig. 3a) was used (Langevin 2008; Vandenbohede et al. 2014).

Implementation of variable flow distribution across the well screen

For the flow close to the well and in the gravel pack, calculated Reynolds numbers indicate that flow is laminar under practical conditions relevant to HT-ATES, and thus the assumption of using Darcy's law is valid (Houben and Hauschild 2011). In this study, to represent the free distribution of inflowing/outflowing water across the well screen, the well was implemented as a column of very high hydraulic conductivity cells in the first column of the model grid (Buscheck et al. 1983). In the top cell of the column representing the well bore, a specified flux boundary (called the 'well package' in MODFLOW software) was used to force the inflow/outflow of water at the top of the well (Fig. 3b). For constant density and viscosity conditions, preliminary simulations showed that assigning the well bore cells with a 2×10^5 times higher K_h value and 1×10^6 times higher K_v than the aquifer led to uniform inflow/outflow distribution for the modelled range of operational conditions and is therefore applied in this study. The simulation models showed that because a highly permeable column was used to represent the well, the well sometimes acts as a preferential flow path for buoyancy-driven flow when the well is not being pumped. Although this is also expected to occur in practice, this has according to currently available sources, not been identified yet in any previous studies on HT-ATES. The SEAWATv4 model output of pressure heads is given in point water head for the location and time-specific temperature of each cell. Therefore, the raw model pressure head output was converted to actual equivalent meter ambient water head relative to the density of the ambient groundwater (Langevin et al. 2008) before being analyzed.

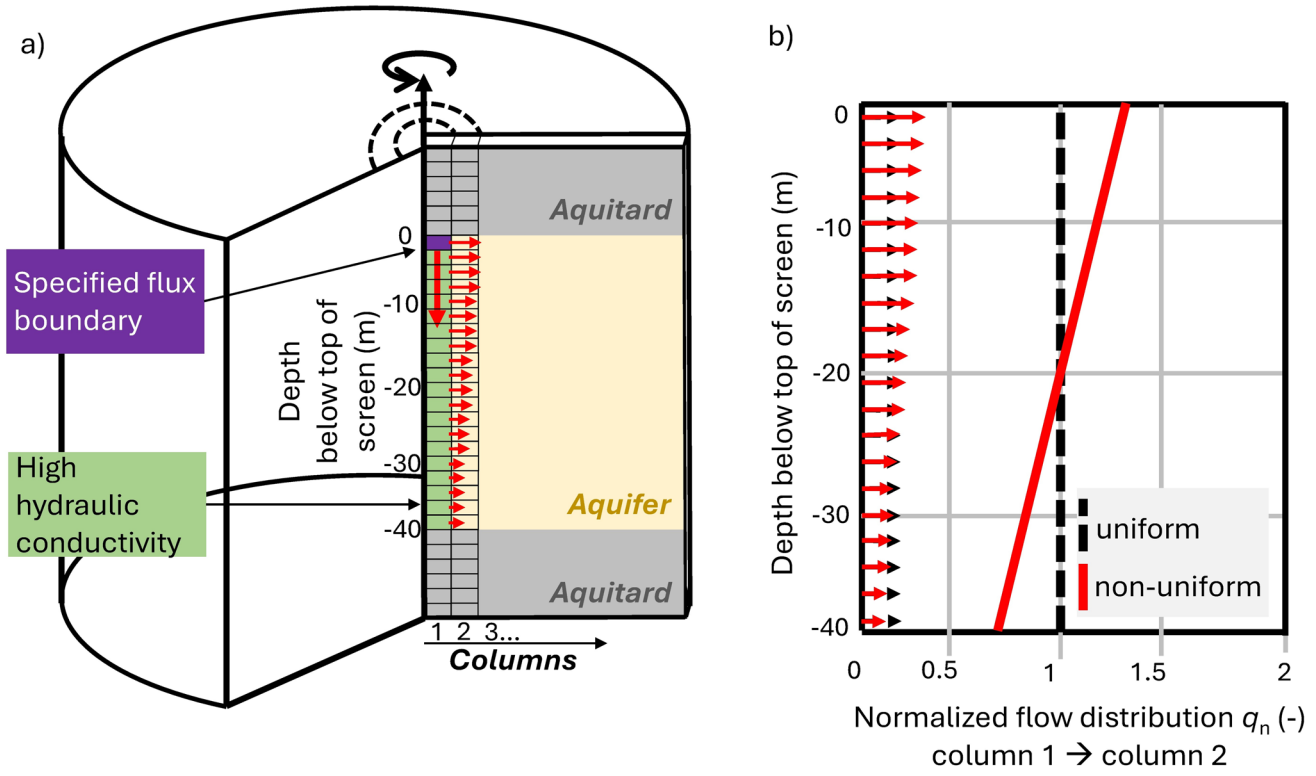

Fig. 3 **a** Schematic overview of the Implementation of the ATES well (column 1) in the axisymmetric model. **b** The average normalized flow distribution is equal to one for uniform flow distribution across the full length of the well screen

Grid, boundary conditions and subsurface properties

The subsurface model is comprised of an aquifer of 40 m thickness, constrained at the top and bottom by an aquitard of 20 m thickness, with homogeneous properties (see Table 1). The vertical grid size used was 0.5 m in the entire model domain, with a horizontal grid size of 0.25 m for the first 10 m of the model, including the well and its close vicinity. Using smaller grid sizes showed negligible differences in flow distribution behavior (< 1% difference) and calculated thermal recovery efficiencies (< 1% difference). After the first 40 horizontal cells (10 m radius), the cell size increases logarithmically until a maximum cell size of 50 m is reached at the boundary of the model at about 750 m from the well. The distance between the well and the outer boundary was tested for larger radii, but no differences were observed. The top, bottom and outer boundary of the model used a constant temperature and constant head boundary. The model was operated with a daily timestep, and for each timestep, the temperature and the inflow/outflow across all cells of the well screen were monitored. Steady-state conditions were used as transient test simulations that included the effect of specific storage, which did not result in different flow distribution or recovery efficiency. Equal volumes were injected and extracted each year, meaning that the well was operated in volume balance. All scenarios were modelled for approximately 5 years (5 × 360 days) using a seasonal 90-day injection-storage-extraction-idle flow scheme. The daily injection/extraction rate used was 1111.1 m^3/day for the base case scenario, resulting in a total storage volume of 100,000 m^3 per well per year.

In the simulations, groundwater was assumed to have a constant specific heat capacity of 4183 J/kg/K and thermal conductivity of 0.58 W/m/K, and an initial temperature of 12 °C. For the entire modelling grid, an effective porosity of 0.3 was used and assumed equal to the total porosity. Groundwater salinity was assumed constant and equal for the entire modelling domain (0 g/L). Within the model, the bulk properties were calculated following the approach of Vandenbohede et al. (2014) for axisymmetric grids. Aquifer hydraulic conductivity (K)/permeability (κ) was assumed to be homogeneous for each layer and anisotropic (anisotropy factor $K_h/K_v = 5$) for the entire modelling grid.

Temperature-dependent water density and viscosity were included in the model (Fig. 4a). For the temperature range considered in this study (12–90 °C), the steepest decrease of viscosity is in the lower temperature range, while for density, the strongest decrease is from 60 to 90 °C (Fig. 4). This nonlinear temperature dependency of both properties is accounted for in the model, with the reference values for 12 °C stated in Table 1. When increasing the temperature from 12 to 90 °C, viscosity decreases 74.8% and density decreases 3.5%, respectively (Fig. 4b).

Model scenarios

A base case scenario was defined for an ATES well with a realistic yearly storage volume (100,000 m^3/year) in a relatively permeable aquifer (K_h = 15 m/day at T = 12 °C, κ_h = 1.87 × 10^{-7} m^2). For the base case scenario, four injection temperatures (15, 30, 60 and 90 °C) were considered to assess the effect of increasing temperature contrasts. For injection at 90 °C, four additional scenarios (scenarios 2–5, Table 2) were assessed that represent different operational conditions (smaller/larger flow rate) or higher/lower aquifer permeability. Additionally, the base case was also simulated with a larger anisotropy ratio of 25 (see scenario 1* in Table 2). To assess the effect of temperature-induced density and viscosity separately, all scenarios were simulated in three ways: (1) constant density and viscosity (not variable with temperature), (2) variable density but constant viscosity, and (3) both variable density and viscosity. Furthermore, all simulations were also executed assuming forced uniform flow distribution across the well screen, during both injection and extraction.

Assessment framework

Normalized flow distribution and pressure head units

The normalized flow distribution across the well screen is determined by dividing the flow per well screen section

Table 1 General hydrogeological layering and properties of the subsurface model implemented in this study. The given K_h and K_v values represent the hydraulic conductivity (m/day) for the base case at ambient groundwater temperature (T = 12 °C); note also that the permeability (κ) is given in m^2

Layer type	K_h (m/day) (at 12 °C) /k (m^2)	K_v (m/day) (at 12 °C) /k (m^2)	Thickness (m)	Effective porosity (-)	Ambient temperature (°C)	Thermal conductivity of solids (W/m/K)	Heat capacity of solids (J/kg/K)
Aquitard	0.001/1.25 × 10^{-11}	0.0002/2.5 × 10^{-12}	20	0.3	12	1.7	710
Aquifer[a]	15/1.87 * 10^{-7}	3/3.75 × 10^{-8}	40	0.3	12	2	710
Aquitard	0.001/1.25 × 10^{-11}	0.0002/2.5 × 10^{-12}	20	0.3	12	1.7	710

[a]Aquifer K_h and K_v were varied for some of the simulated scenarios (see Table 2); all other properties were kept constant

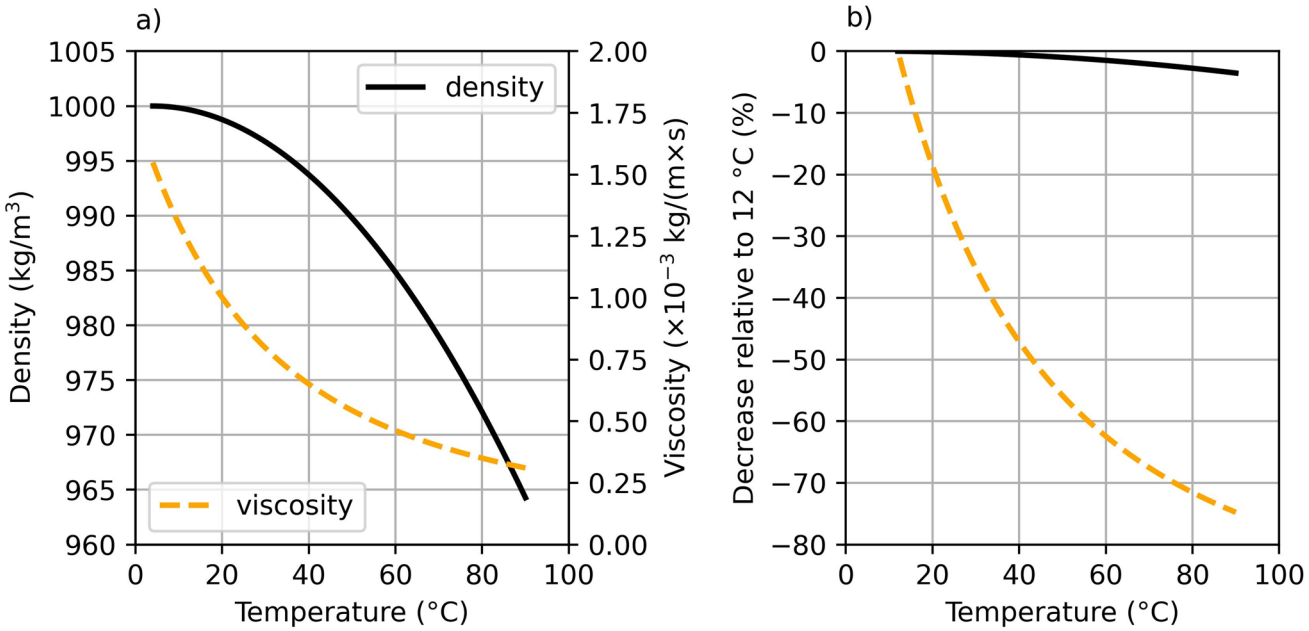

Fig. 4 Nonlinear temperature dependency of density and viscosity (Voss 1984) of water at 1 bar pressure ranging from 12 °C (the ambient groundwater temperature assumed in this study) to 90 °C (the maximum injection temperature simulated)

Table 2 The operational and hydrogeological characteristics of the base case scenario and the varied conditions for the five other scenarios that were included in this study. Increasing Q/K_h is related to higher pressure head conditions in the well (Eq. 1)

Scenario code	Scenario	Injection temperature (°C)	Yearly storage volume (m^3)	Flow rate in/out (m^3/day)	K_h/K_v (m/day, at $T = 12$ °C)	Q/K_h (m^2)
1	Base case	15, 30, 60, 90	100,000	1111	15/3	74
1*	Base case, lower K_v	90	100,000	1111	15/0.6	74
2	High K_h	90	100,000	1111	30/6	37
3	Low K_h	90	100,000	1111	3/0.6	370
4	Larger injection volume	90	250,000	2778	15/3	185
5	Smaller injection volume	90	25,000	278	15/3	19

(0.5 m) by the average flow injected or extracted through the well screen. Hence, when the flow is distributed equally across the well screen, the normalized contribution to flow (q_n) across the length of the well screen is 1 for all parts of the well screen (Fig. 3b). The simulation results showed that the flow distribution across the length of the well screen is very similar for consecutive years of simulation. Therefore, only the results from the first year of the simulations are assessed and presented in the results section. The unit used to describe the pressure conditions in this study is the equivalent pressure head in meters of water pressure (meter head) at the ambient groundwater temperature of $T = 12$ °C ($\rho = 999.7$ kg/m^3); thus, 1-m hydrostatic pressure head is approximately equal to ~0.1 bar.

Recovery efficiency

During injection, the temperature of the inflowing water is constant (T_{inj}). During extraction, the average extracted temperature (T_{out}) for each timestep is the volume-weighted average of the temperature of the water flowing from the aquifer into the well across the screen:

$$\overline{T_{out}}(t) = \frac{\sum_{z=0}^{n} T_{out}(z,t) \cdot q_{out}(z,t)}{\sum_{z=0}^{n} q_{out}(z,t)} \quad (4)$$

where T_{out} is the temperature extracted from the 0.5-m well screen cell, q is the volume flux (m^3/day) per 0.5-m well screen cell, z is the well screen cell number and n is the total number (80) of cells that represent the well (Fig. 2a).

The thermal recovery efficiency of the wells is subsequently calculated as the yearly recovered amount of energy (relative to the ambient groundwater temperature) divided by the yearly amount of energy that was stored during injection (Bloemendal and Hartog 2018):

$$\eta_{th} = \frac{E_{out}}{E_{in}} = \frac{C_w \sum_{t=0}^{n} V_{out}(t) \cdot (\overline{T_{out}}(t) - T_{amb})}{C_w \sum_{t=0}^{n} V_{in}(t) \cdot (T_{in} - T_{amb})} \quad (5)$$

where C_w is the volumetric heat capacity of water (assumed constant at 4,183,000 J/m^3/°C), T_{amb} is the ambient temperature of the aquifer (12 °C), $T_{out/in}$ is the weighted average extracted or injected temperature of the groundwater, and $V_{out/in}$ is the extracted/injected amount of volume during each time step.

Results

Nonuniform flow distribution across the well screen owing to density and viscosity differences

For the simulated base-case scenarios (influenced by temperature-dependent water density and viscosity) with a steady pumping rate of $Q = 1111$ m^3/day, increasing injection temperatures from $T_{inj} = 15$–90 °C results in progressively lower average well screen pressure head (in m equivalent head relative to T_{amb}) during injection and extraction (Fig. 5a), decreasing vertical pressure head distribution with depth in the well screen (Fig. 5b) and nonuniform normalized flow distribution (q_n) across the well screen especially for $T_{inj} = 60$ and 90 °C (Fig. 5c), with increased inflow ($q_n > 1$) at the top of the aquifer and decreased inflow ($q_n < 1$) at the bottom.

For $T_{inj} = 15$ °C, the density and viscosity difference with the ambient groundwater ($T_{amb} = 12$ °C) is negligible, the injection pressure head is constant and equal to the pressure head estimated using Thiem's equation (Eq. 1). At $T_{inj} = 30$, 60 and 90 °C, the average injection pressure head is lower at the start of injection (day 0) but also decreases more during the 90-day injection period as the aquifer fills up with more less-viscous water (Fig. 5a). After 90 days of injection, the average injection pressure head for the 90 °C scenario is only half of the 15 °C scenario. Although the average injection pressure head due to viscosity effects in the well screen is lowest for $T_{inj} = 90$ °C, the density difference compared to the ambient groundwater at $T_{amb} = 12$ °C is considerable ($\Delta\rho = 36$ kg/m^3), resulting in a relatively large injection pressure head Δh_{sim} at the top of the well screen that is larger than the $T_{inj} = 30$ and 60 °C scenarios (shown at $t = 45$ days in Fig. 5b). Also, a more rapidly decreasing pressure head with depth is observed with increasing density differences at higher injection temperatures.

During extraction, the pressure head for the $T_{inj} = 15$ °C is equal (but negative) to the pressure head observed during injection, and hence is again equal to the estimated pressure head using Thiem's equation (Fig. 5a). At $T_{inj} = 30$ °C, similar pressure heads to those found during injection are observed, but as the aquifer gets depleted in time, the viscosity effect becomes smaller and the negative extraction pressure head slightly increases. At $t = 225$ days, the average temperature extracted across the well screen for the $T_{inj} = 30$ °C scenario only slightly decreased to about 27 °C (Fig. 5d), and because of the considerable density difference of the water with the ambient groundwater the pressure head in the well increases with depth, in contrast to the decreasing pressure head during injection (Fig. 5b). Despite the slightly higher pressure head in the bottom (and thus the expected stronger inflow at the bottom), the flow distribution is equal along the depth of the well screen and only the viscosity effect is noticeable at the top and bottom of the well screen (cooling due to conduction at the top and bottom of the aquifer and therefore lower temperatures were extracted there). At 60 and 90 °C, more water is initially injected at the top of the aquifer, and during the 90-day storage period heat has driven upward in the aquifer because of the tilting of the thermal front. Therefore, during extraction, the average pumped temperature is already decreased severely at the start of extraction ($t = 180$ days, Fig. 5d). Only during the first days of extraction, thus representing a relatively small volume, the temperature increased slightly (2 °C) for the scenarios with injection temperatures of 60 and 90 °C, resulting from the relatively colder groundwater that had been transported upward owing to the tilting of the thermal front during storage as the well bore acting as a preferential flow path. After the first days of extraction, the average pumped temperature decreases further during the 90-day period. Hence the viscosity effect on the average extracted pressure head is less than during injection (Fig. 5a) and the vertical pressure head distribution at $t = 225$ days is relatively uniform but slightly higher (more negative) at the bottom of the well screen (Fig. 5b). Nevertheless, the flow distribution at $t = 225$ days (Fig. 5c) is strongly nonuniform with most extraction across the top of the well screen for both the 60 (up to 1.4 normalized flow) and 90 °C (up to 2.2 normalized flow) scenario.

Noticeably, no inflow occurs across the bottom of the well screen (only the first 33 m is used) for $T_{inj} = 90$ °C; however, the bottom of the well screen does have outflow from the aquifer during extraction, albeit a relatively lower share (0.6 normalized flow). The recovered average weighted temperature at the start of extraction for $T_{inj} = 90$ °C is thus influenced by the immediate extraction of cold water from the bottom of the well screen.

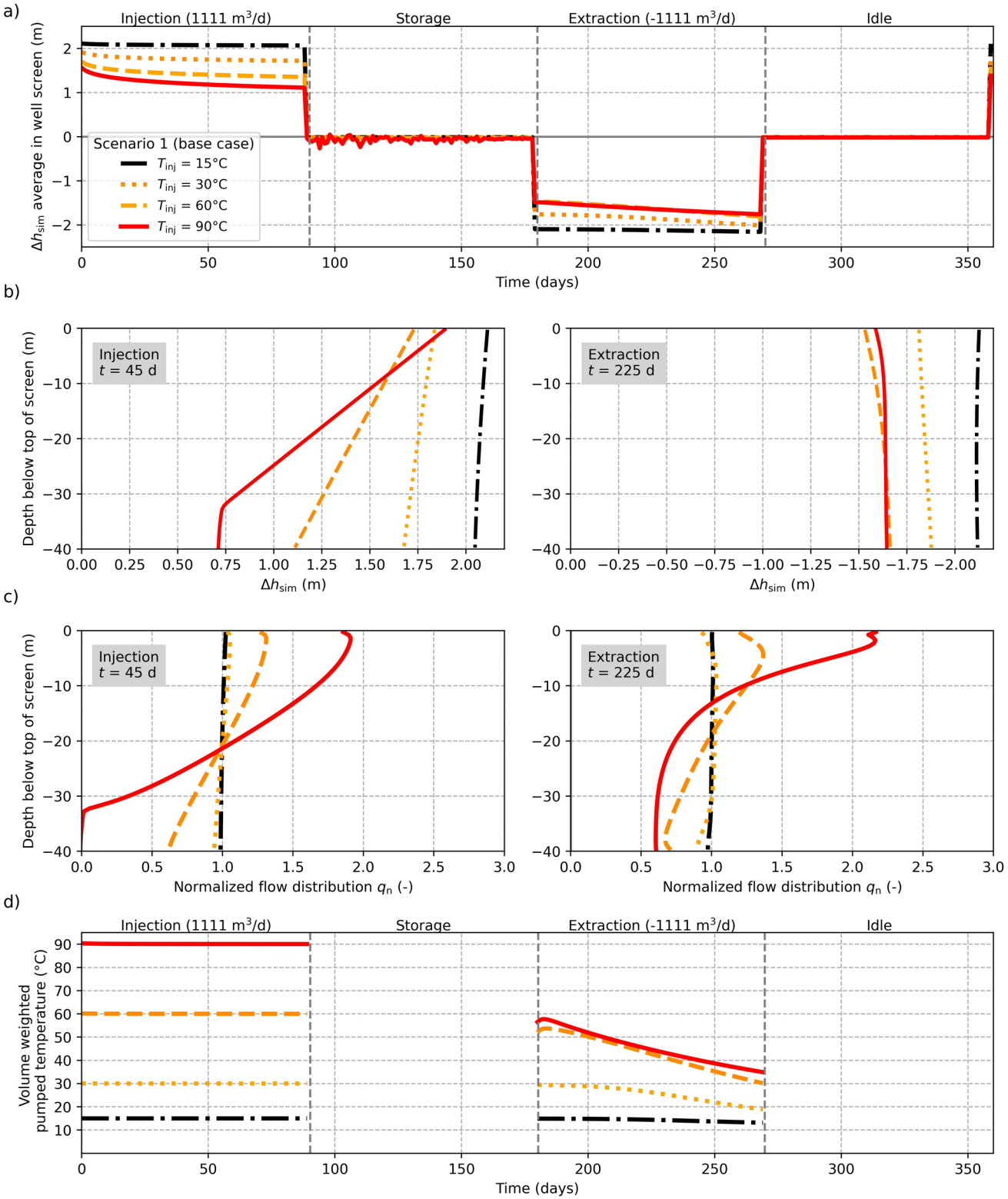

Fig. 5 First-year simulated results for 15, 30, 60 and 90 °C injection temperature (Table 2) at base-case conditions (all equal flow rate and subsurface conditions; Table 1). **a** Average equivalent pressure head in the well screen. **b** Vertical pressure head distribution in the well at $t = 45$ days (halfway injection) and $t = 225$ days (halfway extraction). **c** Normalized flow distribution q_n along the depth of the well screen at $t = 45$ days (halfway injection) and $t = 225$ days (halfway extraction). **d** The volume-weighted pumped temperature injected and extracted with the well

Analytical evaluation of the impact of water density differences at T_{inj} = 90 °C on pressure head differences and flow distribution

Clearly, the vertical injection pressure distribution in the well screen is influenced by the increasing density difference between the injected and ambient groundwater at increasing temperatures (Fig. 5b). Considering uniform steady-state flow from the well and no variable viscosity effects, the average pressure head in the well that is needed to obtain a certain flow from the well to the aquifer is described by Thiem's equation (Eq. 1) and accordingly the average pressure head increases for higher flow rates and lower aquifer transmissivity (as influenced by both hydraulic conductivity and aquifer thickness). However, the vertical distribution of the average pressure head is changed when water is injected with a different density than the ambient aquifer because the hydrostatic pressure of the injected water increases differently with depth compared to the ambient groundwater (Eqs. 2 and 3).

Considering the pressure head difference between two separated columns of water at different densities—one with a relatively low density of $\rho = 964$ kg/m^3 (equal to water of 90 °C) and a reference column with $\rho = 999$ kg/m^3 (density at 12 °C)—the hydrostatic pressure increase with depth in the low-density column is smaller compared to the reference column. If the pressure head at the top of the column with low-density water is increased (similar to injection of hot water; +1 and +5 m, Fig. 6a), the absolute pressure head with the reference (ambient aquifer) decreases with depth (Fig. 6b). Compared to the hydrostatic reference, the pressure head difference at depth D (m) due to the relative density difference ($\Delta\rho_r$), is calculated using Eq. (3). For the column with low-density water with +1-m pressure head at the top, the difference in density ($\Delta\rho = 36$ kg/m^3) with the reference column (ambient groundwater) results in a pressure head that, at a depth of ~28 m, is equal to the hydrostatic pressure in the ambient aquifer. Hence, at that depth, the pressure head difference (Δh) with the aquifer becomes zero, and below this depth, no flow occurs (Fig. 6b, c). For the scenario with 5-m injection pressure head, the pressure head along the 40-m-long well screen also decreases with 0.036 m/m depth, but because at the bottom of the column Δh is still 3.6 m, flow is expected across the entire length of the column (if the columns were connected) causing the normalized pressure head distribution between the two columns to be much closer to the uniform compared to the +1-m pressure head case (Fig. 6c).

When the pressure head is decreased to −1 and −5 m (similar to extraction) at the top of the column,

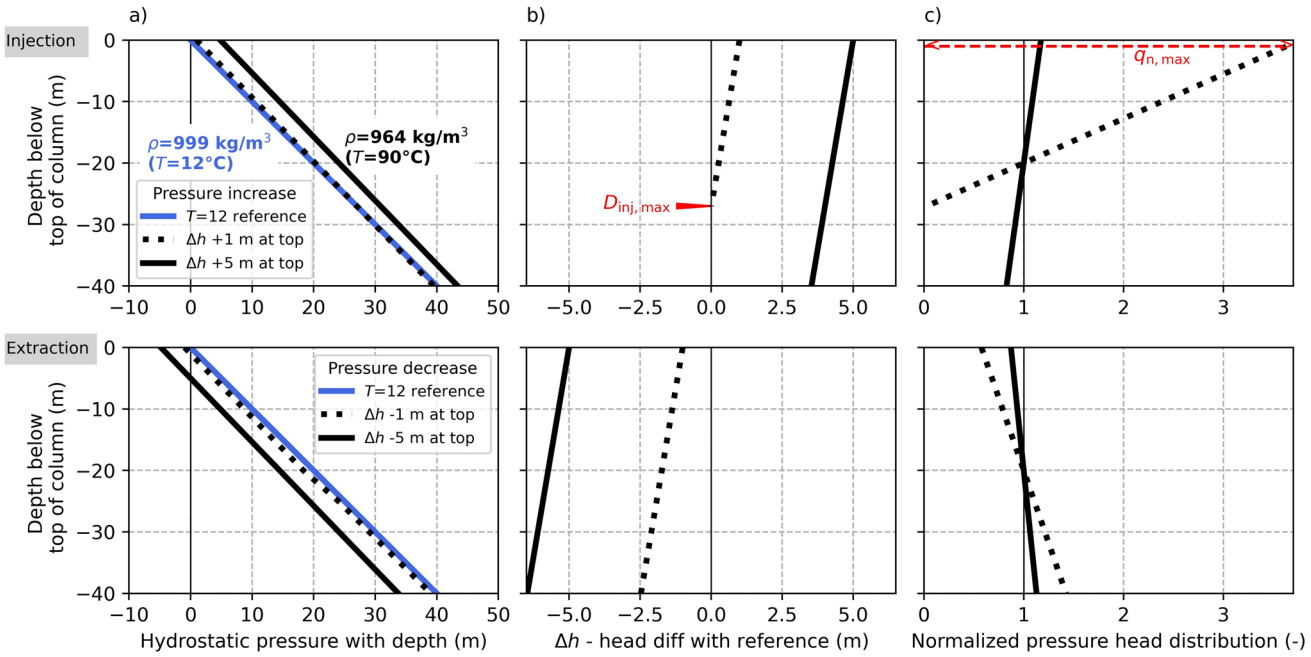

Fig. 6 **a** Theoretical hydrostatic pressure increase (m H_2O at $T = 12$ °C) with depth for two columns of water filled with low-density water ($\rho = 964$ kg/m^3 equal to 90 °C) at 1 and 5-m pressure head and the reference ambient hydrostatic conditions of $\rho = 999$ kg/m^3 (at $T = 12$ °C). **b** The pressure head difference (Δh) with depth between the low-density columns and the reference ($D_{inj,max}$ is the depth where $\Delta h = 0$). **c** The calculated normalized pressure head distribution (based on **b**), with $q_{n,max}$ being the maximum normalized pressure head distribution at the top of the well screen. The top row represents injection (positive pressure head at top of well screen) and the bottom row represents extraction (negative pressure head at top of well screen)

respectively, and assuming that the well is fully filled from top to bottom with the low-density water (ρ = 964 kg/m^3, bottom row of Fig. 6), the hydrostatic pressure head difference between the well and the ambient aquifer increases with depth, opposite to the injection phase. Since the pressure head difference is largest at the bottom, theoretically more flow between the columns would occur in the lower part of the column (if they were connected). Similarly to what is observed when the pressure head is increased at the top, the pressure head difference (Fig. 6b) between the two columns is relatively more nonuniform for the −1-m pressure head; hence, the normalized pressure head distribution is also more nonuniform for the −1-m case compared to the −5-m case. Unlike during head increase of the low-density water (injection), during head decrease (extraction), the pressure difference between the two columns along the length of the columns cannot become zero at any point because the hydrostatic pressure in the low-density column will, in any case, be lower than the column at reference density. Hence, it is expected that with the extraction of low-density water (as with HT-ATES) stored in an ambient aquifer at higher density (e.g., low temperature), there will always be flow across the entire length of the well screen during extraction, which is opposite to injection (Fig. 5c).

The characteristic pressure head decrease Δh_{buoy} (m) at depth D (m) owing to the density difference is dependent on the relative density difference ($\Delta\rho_r$) between the injected (low density) and ambient (higher density) water and is calculated with Eqs. (2) and (3). Similarly, increasing depth results in decreasing pressure head as the injection pressure head is inversely related to the length over which it is injected (Eq. 1). By equating the pressure head calculated with Thiem (Δh_{Thiem}) to the pressure head decrease (Δh_{buoy}), the maximum potential depth of injection for varying relative density difference ($\Delta\rho_r$) and varying storage conditions (Q, K_h) can be calculated:

$$D_{\text{inj,max}} = \sqrt{\frac{Q}{2\pi K_h}\frac{1}{\Delta\rho_r}\ln\left(\frac{R}{r}\right)} \tag{6}$$

Hence, the maximum potential depth of injection ($D_{\text{inj,max}}$) is dependent on the flow rate and hydraulic conductivity, but independent of the actual aquifer depth.

For realistic ranges of $\Delta\rho$ between 0 and 40 kg/m^3 (similar to injecting up to 100 °C in 12 °C aquifer), injection pressure heads as defined by varying flow rate Q (100–2500 m^{3}m/day) and K_h (5–50 m/day, at 12 °C), the maximum theoretical depth of injection $D_{\text{inj,max}}$ varies between < 10 m for low injection pressure conditions (e.g. Q/K = 3) with large $\Delta\rho$ = 40 kg/m^3, to $D_{\text{inj,max}}$ > 300 m for a relatively high injection pressure head conditions (Q/K = 400) and $\Delta\rho$ = 5 kg/m^3 (Fig. 7). For the simulated range of storage conditions (red crosses in Fig. 7) tested in this study (Table 2) the scenario using a relatively high aquifer hydraulic permeability (K_h 30 m/day at T = 12 °C) and the scenario with low injection flow rate (Q; 277 m^{3}m/day) have a relatively low ratio of Q/K (37 and 19 respectively, Table 2) resulting in a calculated maximum depth of injection of 24.4 (scenario 2) and 34.5 m (scenario 5). Hence, for these scenarios, the

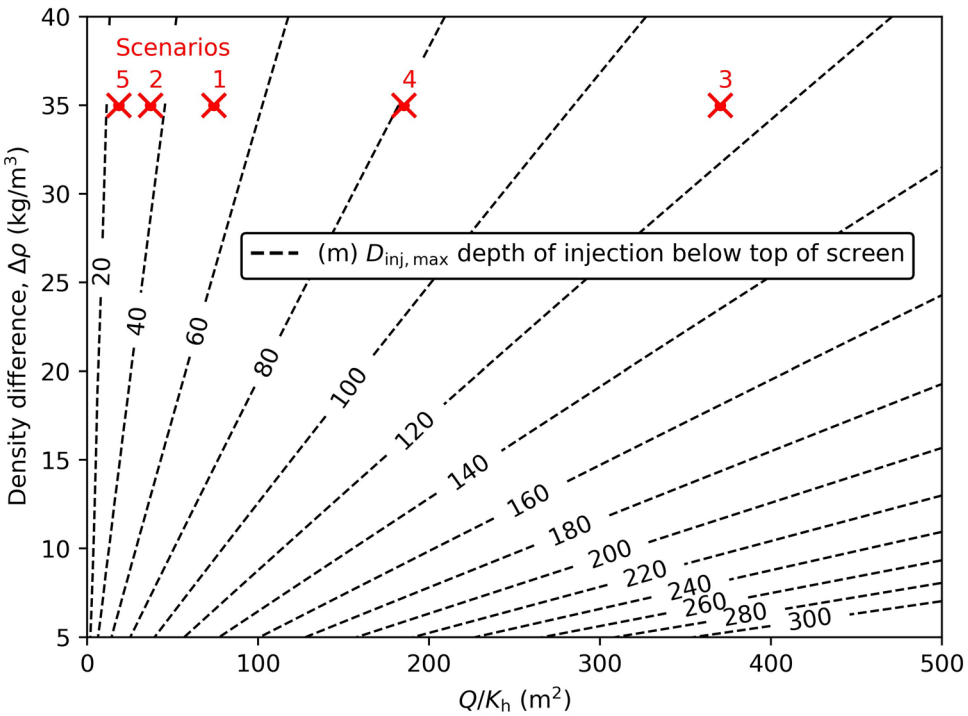

Fig. 7 Theoretically calculated potential maximum depth of injection ($D_{\text{inj,max}}$) for increasing density difference (viscosity effects are not included) between the injected and ambient groundwater (y-axis) for increasing injection pressure heads defined by the ratio of Q/K_h (x-axis). The five scenarios simulated in this study are presented in order of increasing Q/K_h (5, 2, 1, 4, 3) at the density difference of T_{inj} = 90 °C in T_{amb} = 12 °C. For scenarios 5 and 2, $D_{\text{inj,max}}$ is smaller than the aquifer thickness used in this study (40 m)

expected maximum depth of injection below the top of the well screen (calculated using Eq. 9) is smaller than the well screen length of 40 m used in the simulations (only influenced by variable density; viscosity not included).

Simulated flow distributions for T_{inj} = 90 °C during injection when only considering temperature-dependent variable density

For the simulated scenarios that only consider temperature dependent density (viscosity purposely not included), the average pressure head in the well at days 1 and 90 simulated for the different storage conditions considered (Table 2) show good agreement with the calculated pressure heads using Thiem's equation (Fig. 8a). The maximum depth of injection simulated ($D_{inj,sim}$) at the start of injection (day 1) agreed well with the analytically calculated maximum depth of injection ($D_{inj,max}$, Eq. 6). As also observed for the analytically calculated maximum depth of injection (Fig. 7), the simulated depth of injection for scenarios 2 and 5 is above the bottom of the well screen and thus flow only occurs across the upper part of the well screen (Fig. 8b). With time, the simulated depth of injection slightly increases with a few meters as low density water accumulates in the aquifer surrounding the well and the pressure head in the aquifer is slightly decreased.

The normalized flow distribution, resulting from the simulations (at 1, 45 and 90 days of injection, Fig. 9) for the different storage conditions considered, shows decreasing nonuniformity and deeper injection depth with increasing pressure head. The simulation results have good agreement with the analytically calculated normalized pressure distribution based on Eq. (5) (Fig. 6c). The simulations show that initially (day 1) the flow distribution is near-linearly tilted but becomes slightly less nonuniform over time (45 and 90 days), likely due to the progressive heating of the aquifer surrounding the well screen, reducing the density differences in the aquifer. The results show that for a given density difference, flow distribution is increasingly uniform and $D_{inj,sim}$ increases proportionally to the increase of injection pressure head (as a function of increasing Q/K_h, Fig. 7). The simulated depth of injection would be equal to the aquifer thickness (40 m) for Δh_{sim} = 1.4 m according to Eq. (6) and with the larger Δh_{sim}, the nonuniformity increases further with $D_{inj,sim}$ staying equal to the thickness of the aquifer (Fig. 9c–e).

Compared to the flow distribution observed during injection (Fig. 9 top row), the simulated extraction flow distribution at 1, 45 and 90 days (Fig. 9 bottom row) is relatively uniform. Slightly more inflow at the bottom of the screen is observed during the first day of extraction for scenario 1 (Fig. 9c) as the well in that specific scenario is still filled with relatively low-density water at the bottom of the well screen which increases the pressure difference with depth (bottom row in Fig. 6). At days 45 and 90, the bottom of the well screen extracts cold ambient groundwater, and the normalized flow distribution is closer to 1 along the length of the well screen. For scenarios 3 and 4, the flow distribution during injection is relatively uniform owing to the relatively high injection pressure head; hence, during extraction a relatively uniform extraction also occurs, which is slightly less uniform than the injection distribution because of the upward movement of part of the stored heat during storage in the aquifer. For scenarios 2 and 5 (Fig. 9a, b), the well already starts extracting cold water at t = 0 days at the bottom of the well screen partly because there was no low-density water injected during injection and partly because the heat that was initially stored there has moved upward owing to buoyancy-driven flow. Hence, across simulated conditions, the flow

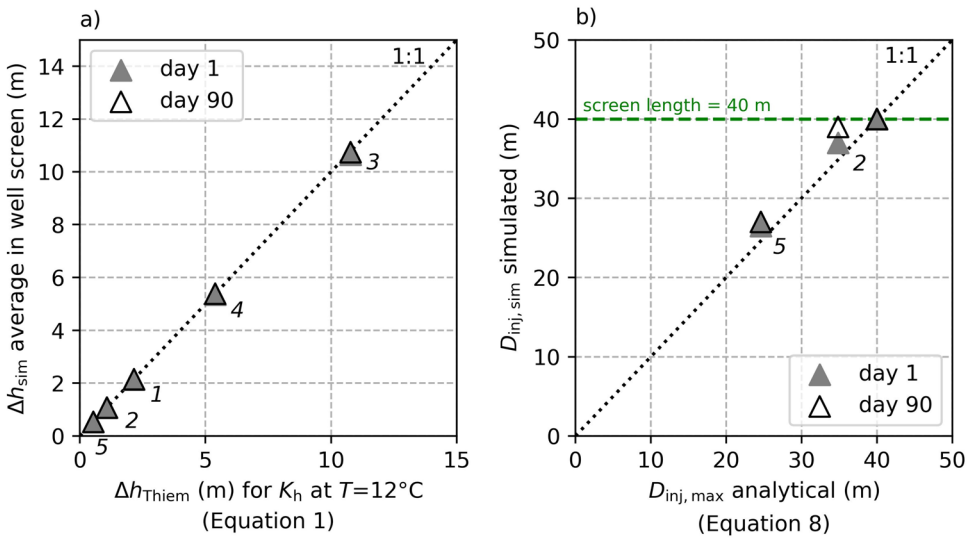

Fig. 8 **a** The expected injection pressure head calculated with Thiem (Eq. 1, for the specific Q, K_h and L = 40) compared to the average injection pressure head in the well screen simulated (variable density, no viscosity) at t = 1 and 90 days for the five scenarios. **b** Calculated maximum depth of injection (Eq. 6), limited by the screen length, equals 40 m, compared to the simulated depth of injection for the five scenarios at t = 1 and 90 days. The numbers 1–5 indicate the scenario numbers

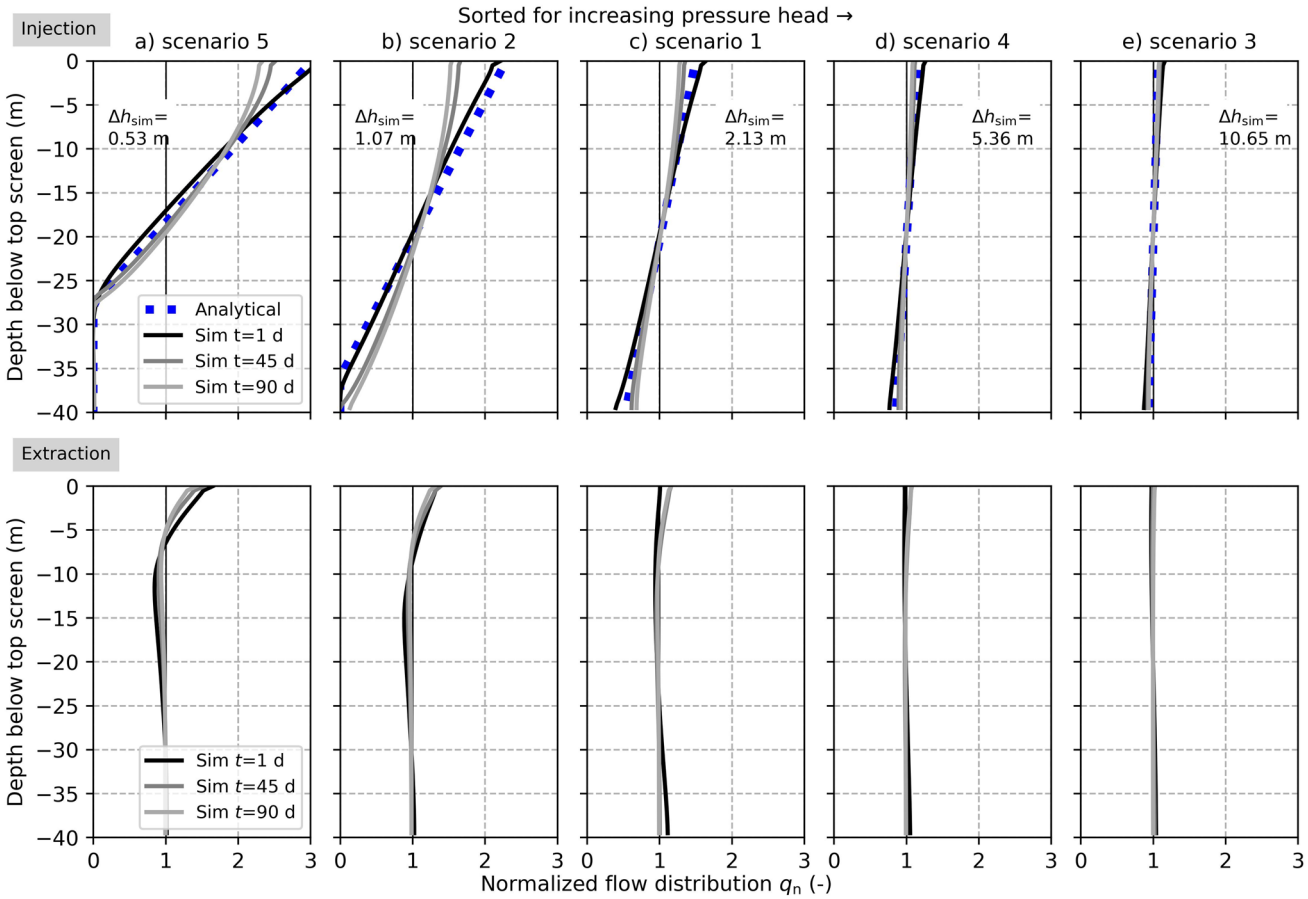

Fig. 9 For the five modelled scenarios (**a**–**e**), in order of increasing injection/extraction pressure head (increasing Q/K_h), the flow distribution across the well screen (top = injection period, bottom = extraction period) at the start of the period (t = 1 day), middle of the period (t = 45 days) and end of the period (t = 90 days). Top row for injection is compared to the analytically calculated pressure distribution, similar to Fig. 6c

distribution at the bottom of the screen during extraction is barely affected by variable density. At the top 5 m of the well screen, slightly more water is extracted because of the presence of relatively low-density water at the top. For scenarios 3 and 4 (Fig. 9d, e), the injection/extraction pressure head is relatively large, and the density difference therefore has only a negligible effect on the vertical pressure head distribution; hence, the flow distribution is close to uniform.

The simulated tilted nonuniform flow distribution during injection (Fig. 9) resulting from the density difference is represented well by the analytically calculated normalized pressure distribution profile (Fig. 6c), while during extraction, the flow distribution is close to uniform for all scenarios (q_n = 1). The fraction injected which flows beyond the uniform normalized flow distribution (q_n = 1) can be considered lost (f_{loss}) when the extracted volume is equal to the injected volume, and is geometrically calculated as a function of the aquifer thickness (L), the relative density factor ($\Delta\rho_r$), the maximum depth of injection ($D_{inj,max}$, Eq. 6) and the average pressure head in the well ($\Delta h_{thiem,}$ Eq. 1), depending on whether the bottom of the screen is reached (Eqs. 7 and 8 in Table 3) or not (Eqs. 9 and 10 in Table 3).

Based on these equations, $D_{inj,max}$, $q_{n,max}$ and the resulting loss fraction are presented in Fig. 10 for a range of pressure head conditions (Q/K_h between 0 and 500) for $\Delta\rho_r$ = 0.036 (at T_{inj} = 90 °C). With increasing Q/K_h, the potential depth of injection increases until $D_{inj,max}$ is equal to the aquifer thickness of 40 m, at Q/K_h = 50 pressure head (Fig. 10a). In this relatively low-pressure range (Q/K_h = 0–50), the normalized maximum flow distribution $q_{n,max}$ at the top of the aquifer decreases exponentially. Although the bottom of the well screen is reached at larger Q/K_h, a further increase in pressure head still leads to a further decrease in $q_{n,max}$. Above Q/K_h = 200, $q_{n,max}$ is smaller than 1.1 and thus the flow distribution across the well screen approaches uniformity. As a result of the larger injection depth and exponentially decreasing nonuniformity of injection, the fraction loss that is geometrically calculated decreases exponentially with increasing Q/K_h, and at Q/K_h = 200 the geometrically

Table 3 Derived equations for the situation when the bottom of the screen is reached ($D_{inj,max} \geq L$) and when it is not reached ($D_{inj,max} < L$) to geometrically calculate the maximum normalized flow distribution at the top of the aquifer during injection (7 and 9) and the fraction loss, geometrically calculated, when it is assumed that during extraction the flow profile is uniform (8 and 10)

Equation No.	Injection conditions	Equation
7	Bottom of the screen is reached, valid when $D_{inj,max} \geq L$	$q_{n,max} = \frac{\Delta h_{Thiem}}{\Delta h_{Thiem} - \frac{L \cdot \Delta \rho_r}{2}}$
8		$f_{loss,geometric} = \frac{(q_{n,max}-1)}{4}$
9	Bottom of the screen is not reached, valid when $D_{inj,max} < L$	$q_{n,max} = \frac{2L}{D_{inj,max}}$
10		$f_{loss,geometric} = \frac{D_{inj,max}}{L} \frac{(q_{n,max}-1)^2}{2q_{n,max}}$

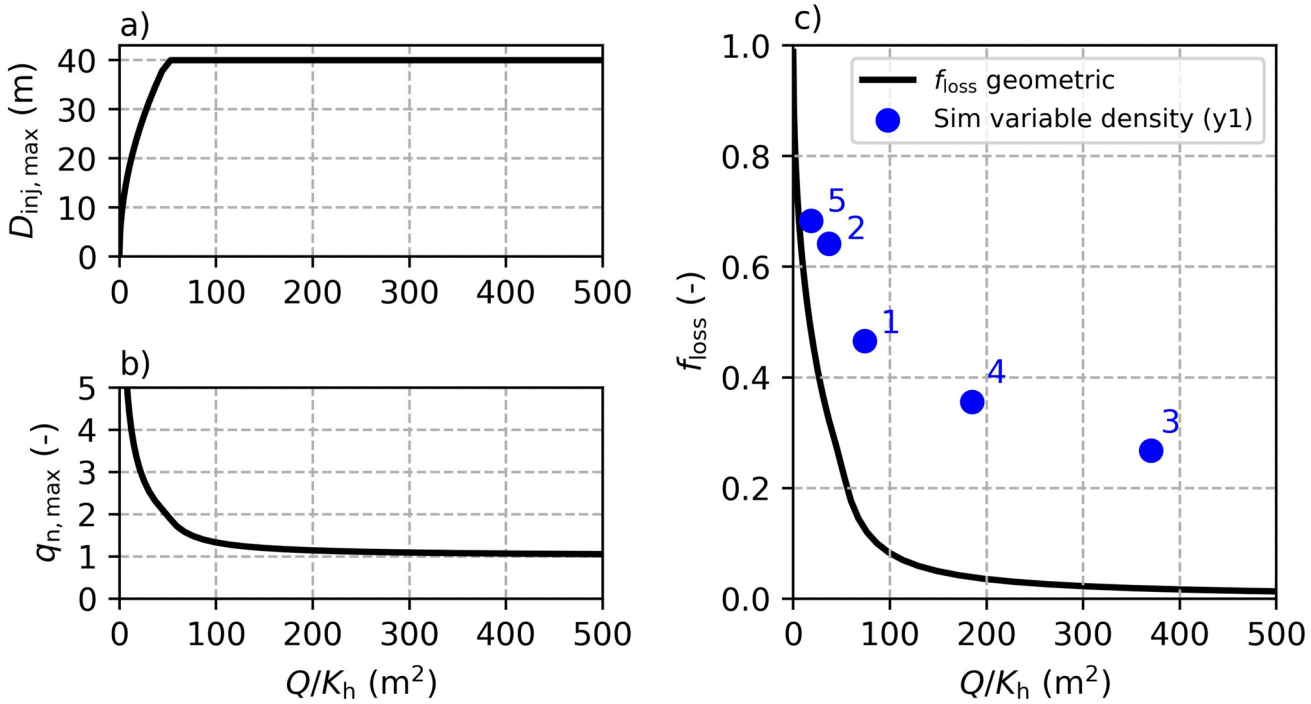

Fig. 10 Increasing Q/K_h (increasing pressure head) **a** calculated increasing maximum depth of injection, **b** the decreasing maximum nonuniform flow factor at the top of the aquifer and **c** the decreasing geometrically calculated loss fraction compared to the simulations (1–5, only considering variable density). For $L = 40$ m and $f_\rho = -0.036$ ($\Delta\rho = 36$ kg/m^3, equal to $T_{inj} = 90$ °C in $T_{amb} = 12$ °C)

calculated fraction loss (Eqs. 8 and 10 in Table 3) is smaller than 0.05 (Fig. 10c). The simulations (variable density only, no viscosity) presented in Fig. 10c show higher fraction loss compared to the geometrically calculated loss fraction as the simulations also include other (time dependent) loss processes such as conduction and buoyancy-driven flow during storage. However, the time-independent loss due to nonuniform injection constitutes a large share of the total loss fraction, especially at small Q/K_h (<30), where it constitutes more than 75% of the total loss fraction simulated in the first year (scenario 5, Fig. 10c).

Simulations at T_{inj} = 90 °C considering temperature dependence for both density and viscosity

Flow distribution nonuniformity increases owing to lowered viscosity at high storage temperatures

When considering variable viscosity, in addition to variable density, for $T_{inj} = 90$ °C for the base case scenario, the increased inflow across the top of the well screen is amplified after the inflow of hot, low-viscosity water has infiltrated the top of the aquifer, surrounding the top of

the well screen. Consequently, this zone with increased apparent hydraulic conductivity results in an even larger fraction of flow of hot water across the top of well screen (Fig. 11). Additionally, the decreased viscosity leads to a lower required average pressure head in the well for a particular injection rate (Δh_{sim} decreases from average 2 to 1.3 m when viscosity is included) leading to an even more nonuniform pressure distribution across the length of the well screen. Hence, the interaction between the relatively lower density and viscosity at $T_{inj} = 90$ °C compared to the aquifer at $T_{amb} = 12$ °C self-reinforces the inflow across the top part of the well screen. During extraction, the zone of relatively low viscosity at the top of the aquifer leads to increased flow across the top part of the well screen (Fig. 11a). At $t = 30$ days, about 3 times more water is extracted from the top 5 m of the well screen (90 °C) compared to the bottom of the well screen where 12 °C ambient groundwater is situated (Fig. 11b). Even though the viscosity effects at the top of the well screen during recovery lead to increased extraction across the top of the well screen, the pressure head difference at the bottom of the well cannot become zero during extraction (Fig. 6b), resulting in the extraction of a significant fraction of relatively cold water from the bottom of the well screen.

Simulated pressure head, flow distribution and thermal recovery efficiency for varying storage conditions

Owing to the injection of low-viscosity water at 90 °C, the pressure head on day 1 is already lower compared to the pressure head calculated with Thiem for K_h at $T_{amb} = 12$ °C (Fig. 12a). Over time, as the aquifer zone around the well fills up with more relatively low-viscosity water (Fig. 12a), the pressure head decreases further. Owing to the lower viscosity, theoretically, when the entire aquifer is fully heated to 90 °C, the pressure head would decrease by a factor of ~4 (red dotted line in Fig. 12a). For the varying simulated scenarios, the pressure head decreases between a factor of 2–3 times after 90 days of injection. As a result of the decreasing pressure heads in time, the simulated depth of injection also decreases in time (Fig. 12b). For scenarios 3 and 4, the injection pressure head is relatively large, and the injection depth is still deeper than 40 m over the entire injection cycle, equal to the simulated depth of injection without viscosity effects (Figs. 8 and 9). Compared to the theoretically (only considering density effects) calculated maximum depth of injection ($D_{inj.max}$), scenario 2 shows already a strongly decreased $D_{inj,sim}$ after 1 day of injection, while for scenario 5, the decrease after 1 day is

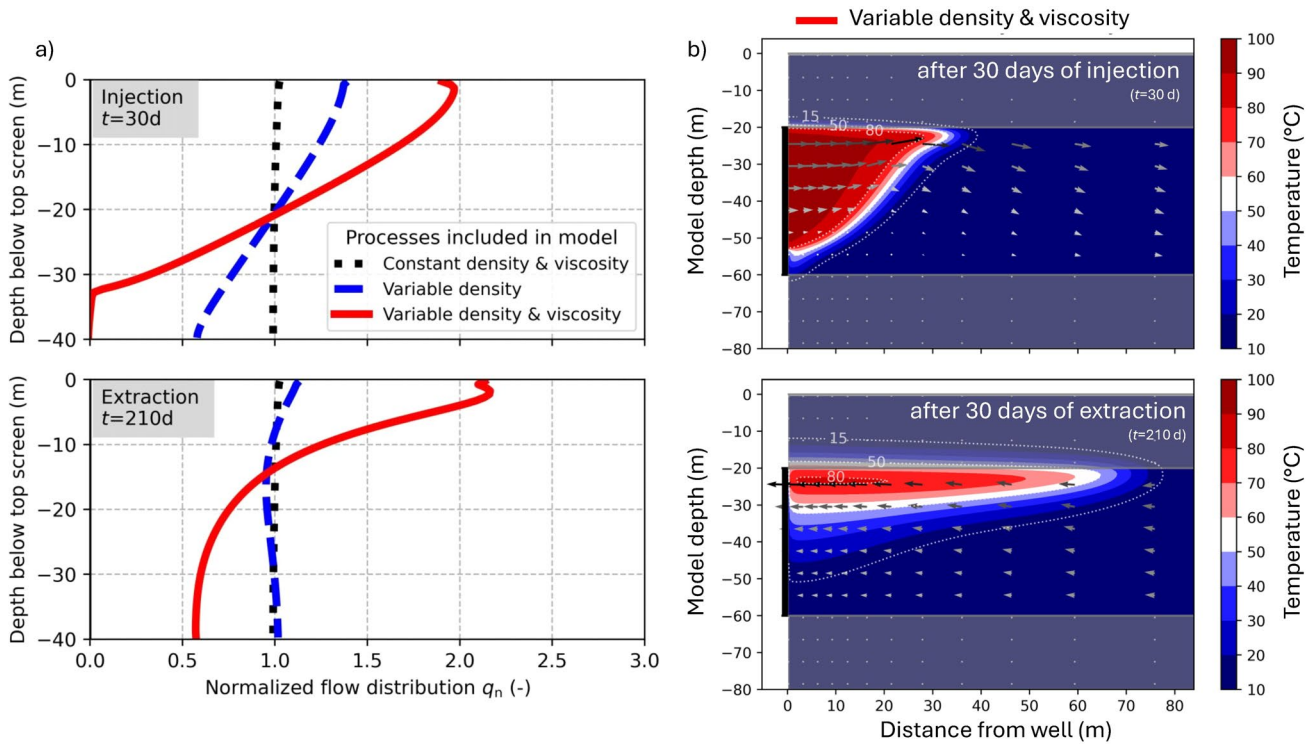

Fig. 11 **a** Flow distribution across the well screen during injection ($t = 30$ days) and extraction ($t = 210$ days) at 90 °C for constant density and viscosity, variable density and both variable density and viscosity simulation. **b** Cross section of the simulated temperature distribution in the aquifer after the first month of injection (top) and after the first month of extraction (bottom) for the simulation including both variable density and viscosity. The magnitude (radially normalized) and direction of flow in the aquifer is indicated by the size, color and direction of the arrows

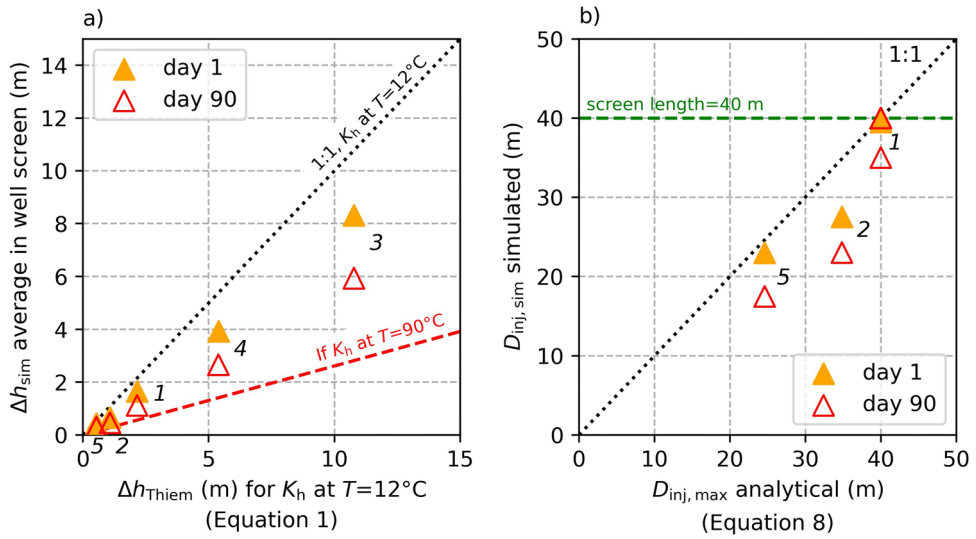

Fig. 12 **a** The analytically calculated (density effects soley) pressure head according to Thiem with $L = 40$ and $\Delta\rho = 0.036$ (x-axis) versus the simulated pressure head (variable density and viscosity) at $t = 1$ and 90 days. The red line indicates the Thiem head calculated for ~4 increased hydraulic conductivity if the aquifer was (entirely) at $T = 90$ °C. **b** The analytically calculated depth of injection according to Eq. (6) and $\Delta\rho = 0.036$ (only density effects) (x-axis) versus the simulated depth (variable density and viscosity) during injection at $t = 1$ and 90 days. The numbers 1–5 indicate the scenario numbers

relatively limited and the depth of injection decreases further (5m) during the 90-day injection period. As scenario 5 has a relatively low injection rate, the viscosity effect due to heating of the aquifer is slower than for scenario 2. For the base case (scenario 1), the simulated injection depth is initially close to the bottom of the well but as the aquifer around the well heats up, the injection depth decreases to about 33 m below the top of the well screen (Figs. 5 and 11).

The average normalized flow distribution for all scenarios is presented (both during injection and extraction) in Fig. 13. Scenarios 2 and 5 with storage conditions that are associated with relatively low injection pressure heads (2: low $Q = 278$ m^{3}m/day and 5: high $K_h = 30$ m/day) show the most nonuniform injection across the well screen resulting in injection solely across the top 25 and 15 m of the well screen respectively (Fig. 13a). The injection flow rates in the top 10 m of the aquifer

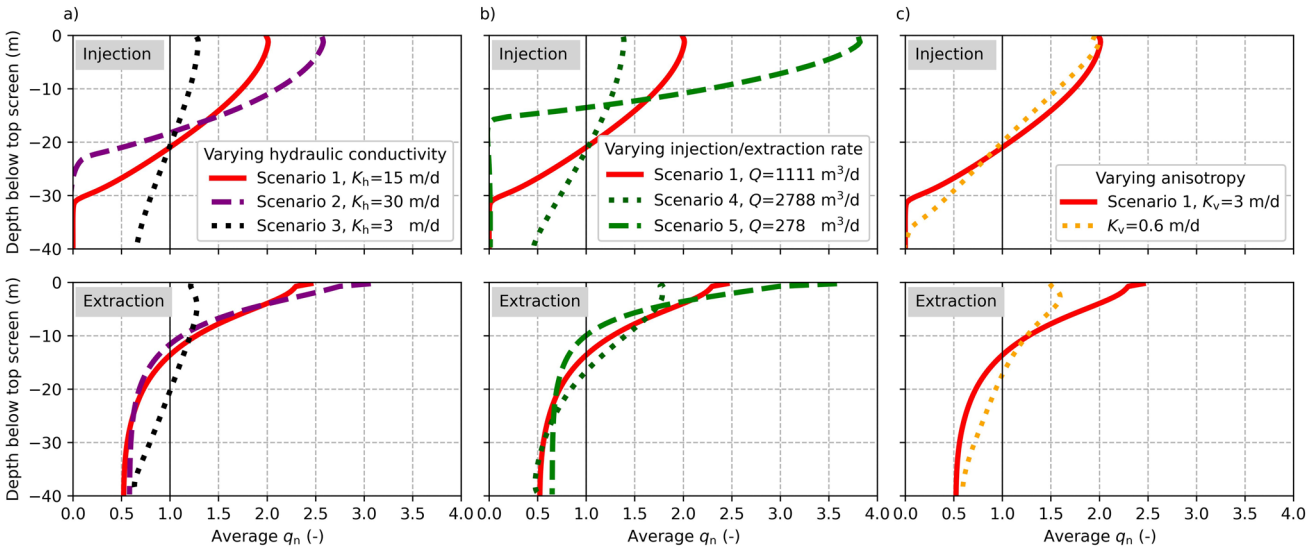

Fig. 13 Average normalized flow distribution (q_n) in year 1 during injection (upper row) and extraction (bottom row) for the base case (red) and the five additional scenarios: **a** varying permeability, **b** varying flow rate, and **c** larger anisotropy factor (lower K_v)

are between 2 to 3.5 times higher than the uniform flow rate distribution. For relatively high well injection pressure heads (scenario 3: low K_h = 3 m/day and scenario 4: high Q = 2778 m^3m/day), the inflow distribution across the well screen is more uniform, ranging from 0.5 at the bottom to 1.5 times the uniform flow rate. Also, during extraction, the nonuniformity of flow distribution is largest for the relatively low pressure head scenarios with most inflow at the top of the well screen due to the effect of low-viscosity water present in the top of the aquifer (Fig. 11b). Clearly however, the differences between the scenarios are much smaller during extraction compared to injection because extraction occurs always across the entire length of the well screen (Fig. 6).

Simulation of the base case scenario with a factor 5 times larger anisotropy factor (K_v = 0.6 m/day) results in very similar (with low K_v slightly deeper injection) average flow distribution during injection as the radial pressure distribution is not influenced substantially by the lowered K_v (Fig. 13c). The slightly deeper injection for the low K_v scenario is likely due to the decreased upward movement of the heat during injection in the lower K_v scenario and, hence, slightly more injection in the bottom of the aquifer. Similarly, low K_v reduced the upward movement of the hot water during the storage period and hence less heat accumulated at the top of the aquifer for the low K_v scenario causing a less nonuniform flow distribution during extraction (max 1.6 times the normalized flow distribution, compared to 2.1 for the base case).

The simulated recovery efficiency at T_{inj} = 90 °C, for both the simulations including variable density and variable density and viscosity, increase for higher pressure head (larger Q/K_h) conditions (Fig. 14). Compared to the simulations that only include variable density, variable viscosity leads to 3–10% lower recovery efficiency in the first year of simulation (Fig. 14). In general, with variable viscosity, the resistance to flow is lowered in the part of the aquifer where most heat is stored (mainly top of the aquifer) and hence relatively more water is injected across the top of the well screen. Moreover, owing to the lowered viscosity, more buoyancy-driven flow occurs during storage (Fig. 11a), contributing to heat loss. On the other hand, during extraction the nonuniformly stored hot water (more at the top of the aquifer) is extracted more efficiently owing to increased extraction from the top of the well screen (Fig. 13). Apparently, as the recovery efficiency is lower when variable viscosity is also included in the simulation (Fig. 14), this compensating effect does not fully compensate for the increased heat losses due to increased nonuniform inflow distribution during injection and the increased upward buoyancy-driven flow during storage that is caused by variable viscosity.

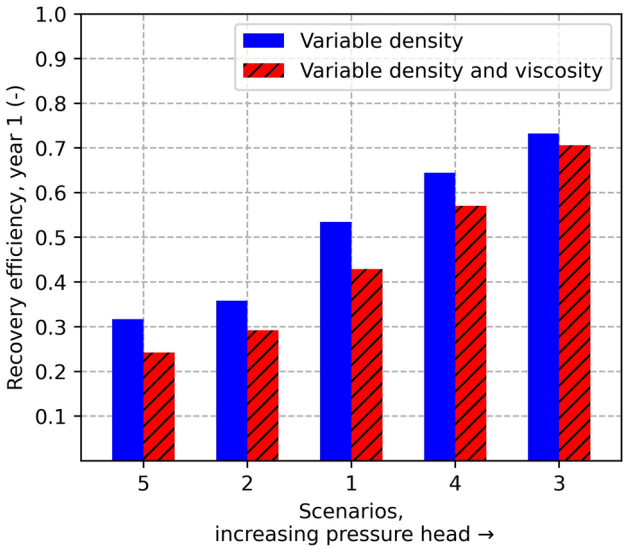

Fig. 14 Simulated first-year recovery efficiency of the five scenarios sorted for increasing pressure head (increasing Q/K_h) for both the simulations, including variable density alone and the simulations taking into account both variable density and viscosity

Discussion

Consideration of nonuniform flow velocities across the borehole wall in HT-ATES design

The strongly nonuniform flow distribution across the well screen owing to density differences and viscosity effects that may occur during HT-ATES operation, as shown in this study (Fig. 13), consequently also leads to a wide range of velocities on the borehole wall (maximum variation for scenario five during injection, between 0 and 3.7 times the uniform velocity). Since the velocity on the borehole wall is a critical design parameter to prevent clogging (Houben 2015a), the occurrence of nonuniform flow conditions is an important consideration in HT-ATES design, as assuming a uniform flow distribution underestimates the maximum flow velocity. For the range of conditions in this study the analytically calculated (only due to variable density) normalized maximum flow distribution at the top of the well screen is between $q_{n,max}$ = 1.1 to 3.1 (–) (Fig. 9). These levels of nonuniformity overlap with the expected nonuniformity under relevant storage conditions tested in previous HT-ATES studies, indicated by the calculated maximum normalized flow distribution and fraction $D_{inj,max}$/L (Fig. 15) for the respective lowest pressure conditions (Q/K_h) that were applied in eight previous studies (cases A–H, calculated based on Q, K_h, L and $\Delta\rho_r$). For each study, the expected most nonuniform flow distribution is shown in Fig. 15. The calculated $q_{n,max}$ and $D_{inj,max}$ (Table 3) should be considered as indicators of the minimum level of

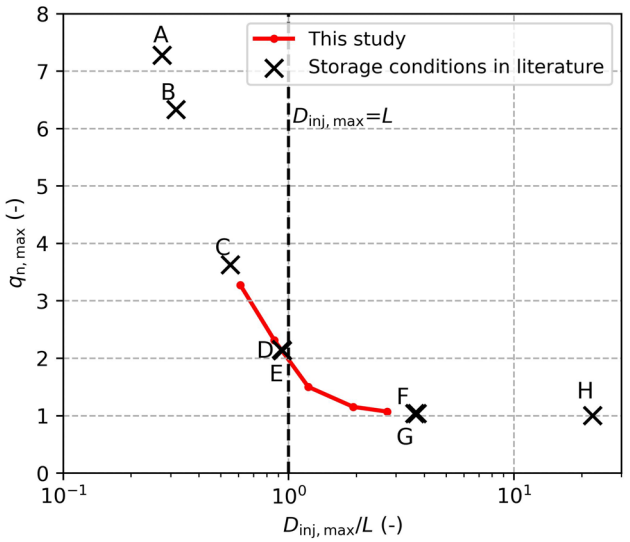

Fig. 15 Calculated nonuniformity parameter $q_{n,max}$ as a function of $D_{inj,max}/L$ (>1 injection occurs across entire well screen) for the range of conditions tested in this study (red dots and line) compared to identified storage conditions applied in literature. The lowest Q/K_h conditions from the literature studies are presented here: **a** Sheldon et al. (2021), **b** Beernink et al. (2024), **c** Heldt et al. (2024), **d** Buscheck et al. (1983), **e** Schout et al. (2014), **f** Wenzlaff et al. (2019), **g** Gao et al. (2019) and **h** Collignon et al. (2020)

nonuniformity since they are solely based on variable density effects and do not take into account the effects of viscosity which further increases the nonuniformity, as shown in this study (e.g. Fig. 11). Although the five yearly cycles simulated for this study did not show significant differences in the flow distribution across the well screen during injection between the consecutive years of simulation (and hence therefore only first year results were shown in the results section), it could be expected that the maximum flow velocity ($q_{n,max}$) at the top of the aquifer would exhibit moderate further increases in time when heat losses build up at the top of the aquifer when for example longer time periods (e.g. 30 years) are simulated or when a cut-off temperature is applied resulting in that only a fraction of the injection volume is extracted. Evaluating the impacts of these kinds of effects on the flow distribution is useful during detailed design of HT-ATES.

Effects of variable flow distribution across the well screen on thermal recovery efficiency

This study showed that, even when considering HT-ATES in a homogeneous aquifer, variable density and viscosity cause nonuniform flow distribution across the well screen, with a larger share of the flow distributed across the top part of the well screen, during both injection and extraction. Some HT-ATES simulation studies (Buscheck et al. 1983; Wenzlaff et al. 2019) used a model setup that allows for variable nonuniform flow distribution, but the flow distribution from the well screens was not discussed. Often, however, studies—e.g. in Beernink et al. (2024); Schout et al. (2014); Sheldon et al. (2021)—use forced uniform flow across the entire well screen (during both injection and extraction), in part for conditions where nonuniform flow is expected to occur based on the insights derived in this study (Fig. 15). For the storage conditions tested in this study, the recovery efficiency was also simulated using forced uniform flow distribution and compared to the simulations using variable flow distribution (Fig. 16). The forced uniform simulations resulted in a recovery efficiency deviation (between +7 and −7%) from the simulations that included variable flow distribution (Fig. 16).

For scenario 3 (K_h = 3 m/day), with the highest pressure-head conditions, the simulated variable in- and outflow pattern was still slightly impacted with a maximum difference of 1.3 q_n at the top of the aquifer (Fig. 13); however, the simulated thermal recovery efficiency for uniform and variable flow distribution was equal for all years simulated (0.7 in year 1 to 0.77 in year (Fig. 16). For scenarios 1, 2, 4 and 5 forced uniform flow distribution resulted in an underestimation of the recovery efficiency between 2 to 7% in year 5. In these cases, forced uniform flow distribution leads to the extraction of a relatively large share of cold water from the bottom of the well screen, which is not compensated for by the previous overestimation of injection through the bottom of the screen (the heat has been transported upwards). However, in the case of relatively low vertical permeability of the aquifer (scenario 1*, Fig. 16), the overestimation of inflow through the bottom is still extractable during the next extraction period because the low K_v impaired the upward movement of the heat. Hence, depending on the subsurface and operational conditions, the simplified modelling assumption of forced uniform flow distribution may result in both an under- and overestimation of the thermal recovery efficiency (although limited to a maximum 7% difference for the tested conditions) compared to models that include nonuniform flow distribution caused by variable density and viscosity. Similar to the low K_v case, assumption of forced uniform flow distribution may lead to an overestimation of the recovery efficiency for smaller storage timescales (e.g. daily storage in Sheldon et al. 2021), because the heat that is (incorrectly) forced to infiltrate at the bottom of the well screen does not have enough time to flow upward (buoyancy-driven flow) and is therefore (incorrectly) extracted again from the bottom of the well screen.

Optimizing well design to increase heat recovery

The results of this study show that the simulations having relatively strong nonuniform flow distribution at low pressure head storage conditions (low Q/K_h; Fig. 13), also have relatively low thermal recovery efficiency (<0.4 in year 5; Fig. 16). Partly this is because flow across the well screen

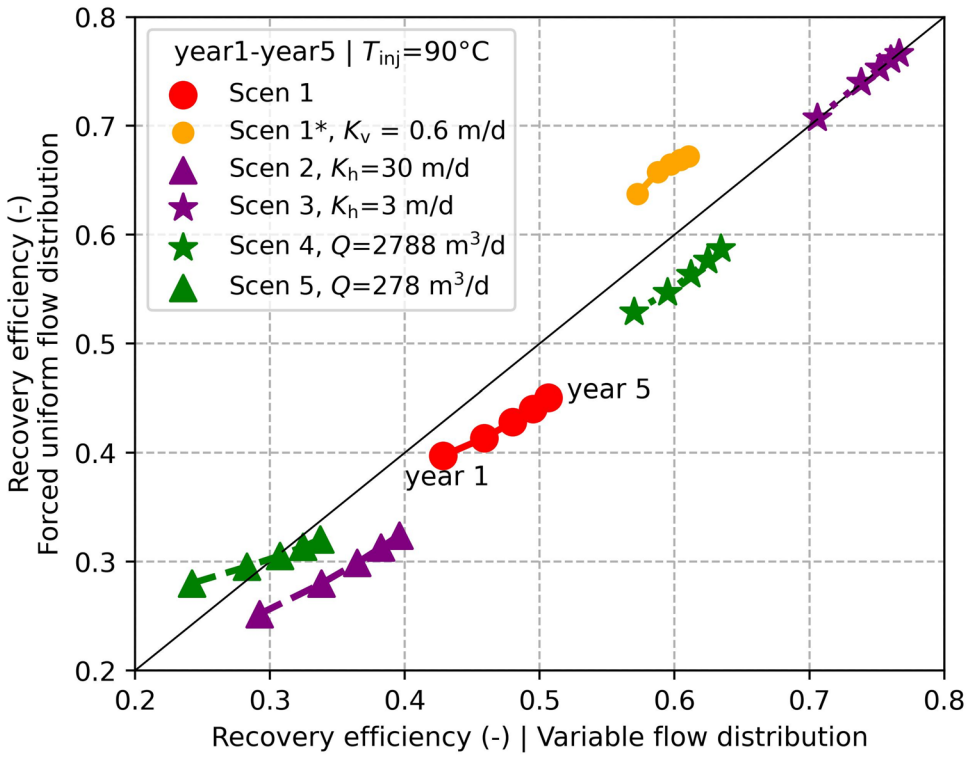

Fig. 16 Simulated recovery efficiency (years 1–5) for the simulations assuming variable nonuniform flow distribution (influenced by density and viscosity, x-axis) versus the same scenarios but simulated assuming forced uniform flow distribution (during both injection and extraction) across the well screen

only occurs in the top part of the well screen during injection ($D_{inj,sim} < L$), which subsequently results in the extraction of cold water from the bottom of the well screen during extraction. Secondly, in low Q/K_h conditions, the flow rate is relatively low (leading to large L/R_{th} storage geometry), or the hydraulic conductivity is relatively high (low resistance to buoyancy-driven flow during storage), and both settings are linked to high thermal losses due to buoyancy-driven flow (Beernink et al. 2024). In practice, the maximum velocity on the borehole wall is generally linked to the horizontal hydraulic conductivity of the aquifer (Houben 2015a; Huisman 1972; Sichardt 1928) and for larger K_h the maximum velocity increases. Hence, to decrease density-difference-initiated losses (both time-independent nonuniform inflow and time-dependent tilting during storage), wells operated close to their maximum flow rate (for a given K_h of the aquifer) have higher recovery efficiency compared to partial load conditions. In practice, relatively large diameter wells (van der Schans et al. 2022) could be used to increase the maximum flow rate for a given aquifer without negatively impacting the velocity on the borehole wall and, hence, decreasing density-difference-initiated heat losses. For conditions where the effects of nonuniform injection and/or buoyancy-driven flow cannot be dealt with by choice of screen length or aquifer selection, a more technical solution like multiple partially penetrating well screens (van Lopik et al. 2022) could be used to increase heat recovery during extraction.

Impact of permeability heterogeneity of the storage aquifer

The results of this study have shown that for the density and viscosity differences that occur under common HT-ATES conditions, buoyancy-induced nonuniform flow distributions across the well screen during injection and extraction can be expected, as was highlighted by assuming a homogeneous aquifer. In contrast, nonuniform flow across well screens resulting from (layered) permeability variations due to aquifer heterogeneity (e.g. 1–2 orders of magnitude) is of course well-known in the field of hydrogeology, including HT-ATES (Bridger and Allen 2014; Buscheck et al. 1983; Heldt et al. 2024; van Lopik et al. 2022). However, whereas permeability variations affect the flow distribution equally during injection and extraction, buoyancy-induced nonuniform flow is shown to be asymmetrical during injection and extraction, i.e., during injection most or all is infiltrated at the top of the aquifer while extraction always occurs across the full well screen length, therefore affecting recovery efficiency (Fig. 5). However, for HT-ATES in heterogeneous aquifers, the variation in permeability will interact with the temperature-dependent effects on buoyancy and viscosity and therefore affect the overall flow distribution. An example of this would be that, for HT-ATES in an aquifer with a coarsening upward sequence, resulting in higher permeabilities at the top of the aquifer (Reading 2009), the buoyancy induced nonuniformity would be amplified, while conversely, in an

aquifer with a fining-upward sequence, this nonuniformity would be dampened. For HT-ATES in aquifers with more complex heterogeneities, it will be more difficult to anticipate the resulting flow distributions during injection and extraction and the resulting effect on recovery efficiencies; thus, the use of multiple partially penetrating wells might be required to allow more targeted infiltration and extraction and facilitate more efficient recovery (van Lopik et al. 2022). For the simulations done in this study of HT-ATES, forcing uniform flow across the well screen during infiltration caused relatively small errors in the resulting recovery efficiencies (Fig. 16), as the too deeply infiltrated hot water will still relatively easily equilibrate with the actual density-dependent pressure conditions once in the aquifer. However, these errors will be larger with increasing heterogeneity, as forcing infiltration, particularly under deeper and lower permeability layers will hamper the correction towards the pressure equilibrium of the erroneously deep injected hot water. Therefore, particularly for the simulation of HT-ATES in heterogeneous aquifers, it is advisable to allow buoyancy-induced nonuniform flow distribution across the well screen.

Similarity and relevance for subsurface freshwater storage

The occurrence of nonuniform flow distribution, as assessed in detail for HT-ATES in this study, has also been observed for other types of subsurface injections with varying fluid densities and viscosities, e.g., CO_2 (Pegler et al. 2014; Taku Ide et al. 2007). However, the effect of nonuniform flow distribution on the intrinsic aim of recovering the stored fluid (such as with HT-ATES in this study) has not been analyzed before. Another type of variable-density subsurface injection and recovery of water involves the injection and recovery of freshwater when performing aquifer storage and recovery (ASR) in saline/brackish aquifers. With typical ASR systems in practice (Ward et al. 2007; Zuurbier et al. 2014), similar density differences ($\Delta\rho$ in the range of 5–25 kg/m^3) occur as the tested HT-ATES conditions in this study (Fig. 7). Although many ASR studies (Kumar and Kimbler 1970; Peters 1983; Zuurbier et al. 2014) note that at low pumping rates the injected freshwater is affected more strongly by the effects of the density difference, this effect is only related to the (time-dependent) vertical upward buoyancy-driven flow in the aquifer and not to the (time-independent) effect of buoyancy dependent nonuniform injection of the fresh water across the well screen. Unlike for the storage of hot water with HT-ATES, no significant viscosity differences are involved with the storage of freshwater in saline aquifers, and hence the simulations in this study that only accounted for variable density (e.g. Fig. 9) would be most representative for the functioning of ASR systems; thus, the analytically determined parameters that indicate buoyancy-induced nonuniformity during injection, and the geometrically equation to calculate the loss fraction (Table 3), would be relevant for such ASR systems. Therefore, further research into the specific conditions and effects of buoyancy-induced nonuniform injection and recovery in ASR systems appears well justified.

Conclusions

In this research, buoyancy-induced nonuniform flow distribution across the screen of HT-ATES wells was investigated under relevant storage conditions using variable density and viscosity groundwater flow simulations that allowed the variable distribution of flow across the well screen in an aquifer of 40 m thickness. The numerical simulations, supported by analytical analysis, showed that increasing injection temperatures (15, 30, 60 and 90 °C) in a relatively cold ambient aquifer (12 °C) made the flow distribution across the well screen increasingly nonuniform. This was the case both during injection and extraction, with the highest normalized flow distribution (q_n) found across the top part of the well screen, which was up to multiple times the average flow rate across the length of the well screen ($q_n = 1$).

Simulations that only included the effect of variable density (viscosity purposely not included) at $T_{inj} = 90$ °C showed that nonuniform injection is caused by the density difference between the injected and ambient groundwater. Additionally, it was found that the degree of nonuniformity (expressed as the maximum normalized flow distribution $q_{n,max}$ at the top of the aquifer and the maximum depth of injection $D_{ini,max}$) increases with decreasing pressure head conditions (decreasing Q/K_h). Analytical formulations were derived that allow for the calculation of expected nonuniformity and the fraction loss due to (time-independent) nonuniform injection caused by the density difference between the injected and ambient groundwater for varying conditions. For the five storage conditions tested, the two scenarios with the lowest Q/K_h resulted in a maximum injection depth above the bottom of the well screen ($D_{inj,sim} < L$), while the maximum simulated $q_{n,max}$ was above 2.5 times the uniform flow rate. Although results show that the analytical formulations accurately estimate $D_{inj,max}$ and $q_{n,max}$ of the simulated scenarios, the loss fractions analytically calculated are lower because, in the simulations, additional (time-dependent) heat loss processes are included such as conduction and buoyancy-driven flow during storage. However, especially for situations where injection is strongly nonuniform ($Q/K_h < 50$ m^2), the (time-independent) loss fraction owing to nonuniform injection, which is analytically calculated, constitutes up to 75% of the total loss in year 1.

The decreasing viscosities with higher injection temperatures further amplify the nonuniform flow distribution due to increasing density differences, as the progressing inflow of heat in the top of the aquifer creates a zone of lower hydraulic resistance, which increases the inflow further. As a result, inflow for the simulations at the lowest Q/K_h (<50 m^2) tested only occurred through the upper 40–50% of the well screen. Although based soley on density difference, a relatively uniform flow distribution is expected during extraction, and viscosity effects result in increased outflow at the top of the well screen. Regardless of conditions, however, flow distribution during injection and extraction is always asymmetrical as, in contrast to injection, extraction will always induce flow across the full well screen length.

In addition to contributing to heat losses, the extent to which nonuniform flow distribution across the well screen occurs consequently also results in substantially higher maximum velocities across the borehole wall during both injection and extraction. These maximum velocities, which are a critical design parameter to prevent clogging, were up to 3.7 times higher (for the conditions tested) than for the typical assumption of forced uniform flow distribution.

Key insights from this study are that temperature-induced variable density and viscosity intrinsically lead to nonuniform flow distribution across the well screen, that is intrinsically different during injection and extraction, contributing to the loss of heat recovery. Moreover, the induced elevated flow velocities across parts of the well screen potentially lead to increased clogging risks. Overall, an assessment of the storage conditions in practice as derived from previous studies indicates that the occurrence of nonuniform flow distribution is an aspect that should generally be considered in HT-ATES design.

Acknowledgements We would like to thank our colleagues at KWR Water Research and Delft University of Technology for valuable discussions and their constructive feedback. The authors thankfully acknowledge the financial support of RVO and the WarmingUP GOO project. Lastly, we would like to thank two anonymous reviewers for their valuable comments.

Author contributions All authors contributed to the study conception and design. Literature review, simulation setup, numerical modelling and initial analysis of the data were performed by Stijn Beernink. Together with Niels Hartog, Martin Bloemendal and Philip J. Vardon, the results were analyzed and processed. The analytical/geometrical analysis was done by Stijn Beernink and Niels Hartog. The first draft of the manuscript was written by Stijn Beernink and all authors commented on previous versions of the manuscript. All authors read and approved the final manuscript.

Funding This research was supported by the Dutch project WarmingUP GOO, which aimed to accelerate the application of geothermal energy and underground heat storage. The WarmingUP GOO project (MOOI322012) is funded in the MOOI program of RVO in the Netherlands, with subsidy scheme number TSE-22-22-03.

Rijksdienst voor Ondernemend Nederland, MOOI322012, Niels Hartog.

Data availability All produced (simulation) data is available from the author on request.

Declarations

Ethics approval Not applicable.

Consent to participate Not applicable.

Consent for publication Not applicable.

Competing interests The authors declare that they have no known competing financial interests or personal relationships that could have appeared to influence the work reported in this paper.

Open Access This article is licensed under a Creative Commons Attribution 4.0 International License, which permits use, sharing, adaptation, distribution and reproduction in any medium or format, as long as you give appropriate credit to the original author(s) and the source, provide a link to the Creative Commons licence, and indicate if changes were made. The images or other third party material in this article are included in the article's Creative Commons licence, unless indicated otherwise in a credit line to the material. If material is not included in the article's Creative Commons licence and your intended use is not permitted by statutory regulation or exceeds the permitted use, you will need to obtain permission directly from the copyright holder. To view a copy of this licence, visit http://creativecommons.org/licenses/by/4.0/.

References

Bakker M, Post V, Langevin CD, Hughes JD, White JT, Starn JJ, Fienen MN (2016) Scripting MODFLOW model development using Python and FloPy. Groundwater 54(5):733–739. https://doi.org/10.1111/gwat.12413

Beernink S, Hartog N, Vardon PJ, Bloemendal M (2024) Heat losses in ATES systems: the impact of processes, storage geometry and temperature. Geothermics 117:102889. https://doi.org/10.1016/j.geothermics.2023.102889

Birdsell DT, Adams BM, Saar MO (2021) Minimum transmissivity and optimal well spacing and flow rate for high-temperature aquifer thermal energy storage. Appl Energy 289:116658. https://doi.org/10.1016/j.apenergy.2021.116658

Bloemendal M, Hartog N (2018) Analysis of the impact of storage conditions on the thermal recovery efficiency of low-temperature ATES systems. Geothermics 17:306–319. https://doi.org/10.1016/j.geothermics.2017.10.009

Bloemendal M, Vardon PJ, Medema A, Snelleman S, Marif K, Beernink S, Van Veldhuizen F, Pijnenborg M, Sudintas G, Van Oort T (2020) Feasibility study HT-ATES at the TU Delft campus. https://www.warmingup.info/documenten/window-fase-1---a1---verkenning-hto-tud---feasibilityht_ates_tudelft.pdf. Accessed August 2026

Bridger DW, Allen DM (2014) Influence of geologic layering on heat transport and storage in an aquifer thermal energy storage system. Hydrogeol J 22(1):233–250. https://doi.org/10.1007/s10040-013-1049-1

Buscheck TA, Doughty C, Tsang CF (1983) Prediction and analysis of a field experiment on a multilayered aquifer thermal energy storage system with strong buoyancy flow. Water Resour Res 19(5):1307–1315. https://doi.org/10.1029/WR019i005p01307

Collignon M, Klemetsdal ØS, Møyner O, Alcanié M, Rinaldi AP, Nilsen H, Lupi M (2020) Evaluating thermal losses and storage capacity in high-temperature aquifer thermal energy storage (HT-ATES) systems with well operating limits: insights from a study-case in the Greater Geneva Basin, Switzerland. Geothermics 85:101773. https://doi.org/10.1016/j.geothermics.2019.101773

Craig F Jr, Sanderlin J, Moore D, Geffen T (1957) A laboratory study of gravity segregation in frontal drives. Transactions of the AIME 210(01):275–282. https://doi.org/10.2118/676-G

Dobson P, McLing T, Spycher N, Fleuchaus P, Neupane G, Doughty C, Zhang Y, Smith R, Atkinson T, Jin W, Blum P, Dinkelman D, Veldkamp H (2025) High-temperature aquifer thermal energy storage (HT-ATES) projects in Germany and the Netherlands: review and lessons learned. Energies 18(23):6292. https://doi.org/10.3390/en18236292

Doughty C, Hellström G, Fu Tsang C (1982) A dimensionless parameter approach to the thermal behavior of an aquifer thermal energy storage system. Water Resour Res 18(3):571–578. https://doi.org/10.1029/WR018i003p00571

Fleuchaus P, Godschalk B, Stober I, Blum P (2018) Worldwide application of aquifer thermal energy storage: a review. Renew Sustain Energy Rev 94:861–876. https://doi.org/10.1016/j.rser.2018.06.057

Fleuchaus P, Schüppler S, Bloemendal M, Guglielmetti L, Opel O, Blum P (2020) Risk analysis of high-temperature aquifer thermal energy storage (HT-ATES). Renew Sustain Energy Rev 133:110153. https://doi.org/10.1016/j.rser.2020.110153

Gao L, Zhao J, An Q, Liu X, Du Y (2019) Thermal performance of medium-to-high-temperature aquifer thermal energy storage systems. Appl Therm Eng 146:898–909. https://doi.org/10.1016/j.applthermaleng.2018.09.104

Han J, Lee M, Lee W, Lee Y, Sung W (2016) Effect of gravity segregation on CO_2 sequestration and oil production during CO_2 flooding. Appl Energy 161:85–91. https://doi.org/10.1016/j.apenergy.2015.10.021

Harbaugh AW, Banta ER, Hill MC, McDonald MG (2000) MODFLOW-2000, the US Geological Survey modular ground-water model: user guide to modularization concepts and the ground-water flow process. US Geological Survey, Reston, VA

Heldt S, Beyer C, Bauer S (2024) Uncertainty assessment of thermal recovery and subsurface temperature changes induced by high-temperature aquifer thermal energy storage (HT-ATES): a case study. Geothermics 122:103086. https://doi.org/10.1016/j.geothermics.2024.103086

Hellström G, Tsang C-F, Claesson J (1988) Buoyancy flow at a two-fluid interface in a porous medium: analytical studies. Water Resour Res 24(4):493–506. https://doi.org/10.1029/WR024i004p00493

Henry A, Prasher R, Majumdar A (2020) Five thermal energy grand challenges for decarbonization. Nat Energy 5(9):635–637. https://doi.org/10.1038/s41560-020-0675-9

Houben G (2015a) Review: Hydraulics of water wells—flow laws and influence of geometry. Hydrogeol J. https://doi.org/10.1007/s10040-015-1312-8

Houben G (2015b) Review: Hydraulics of water wells—head losses of individual components. Hydrogeol J. https://doi.org/10.1007/s10040-015-1313-7

Houben GJ, Hauschild S (2011) Numerical modeling of the near-field hydraulics of water wells. Ground Water 49(4):570–575. https://doi.org/10.1111/j.1745-6584.2010.00760.x

Huisman L (1972) Groundwater recovery and recharge. Macmillan, New York

Kumar A, Kimbler OK (1970) Effect of dispersion, gravitational segregation, and formation stratification on the recovery of freshwater stored in saline aquifers. Water Resour Res 6(6):1689–1700. https://doi.org/10.1029/WR006i006p01689

Langevin CD (2008) Modeling axisymmetric flow and transport. Groundwater 46(4):579–590. https://doi.org/10.1111/j.1745-6584.2008.00445.x

Langevin, CD, Thorne DT, Dausman AM, Sukop MC, Guo W (2008) SEAWAT Version 4: a computer program for simulation of multi-species solute and heat transport. US Geological Survey, Reston, VA

Mindel JE, Alt-Epping P, Landes AAL, Beernink S, Birdsell DT, Bloemendal M, Hamm V, Lopez S, Maragna C, Nielsen CM, Olivella S, Perreaux M, Saaltink MW, Saar MO, Van den Heuvel D, Vidal R, Driesner T (2021) Benchmark study of simulators for thermo-hydraulic modelling of low enthalpy geothermal processes. Geothermics 96:102130. https://doi.org/10.1016/j.geothermics.2021.102130

Pegler SS, Huppert HE, Neufeld JA (2014) Fluid injection into a confined porous layer. J Fluid Mech 745:592–620

Peters JH (1983) The movement of fresh water injected in salaquifers. KIWA, Nieuwegein, The Netherlands

Post V, Kooi H, Simmons C (2007) Using hydraulic head measurements in variable-density ground water flow analyses. Groundwater 45(6):664–671

Reading HG (2009) Sedimentary environments: processes, facies and stratigraphy. Wiley, Chichester, England

Schout G, Drijver B, Gutierrez-Neri M, Schotting R (2014) Analysis of recovery efficiency in high-temperature aquifer thermal energy storage: a Rayleigh-based method. Hydrogeol J 22(1):281–291. https://doi.org/10.1007/s10040-013-1050-8

Sheldon HA, Wilkins A, Green CP (2021) Recovery efficiency in high-temperature aquifer thermal energy storage systems. Geothermics 96:1–18. https://doi.org/10.1016/j.geothermics.2021.102173

Sichardt W (1928) Das Fassungsvermogen von Rohrbrunnen und Seine Bedeutung Fur Die Grundwasserabsenkung, Insbesondere Fur große Absenkungstiefen [The water intake capacity of tube wells and its importance for the lowering of groundwater level, especially for larger drawdowns]. Springer, Heidelberg, Germany. https://doi.org/10.1007/978-3-642-92262-6_2

Sommer WT, Doornenbal PJ, Drijver BC, van Gaans PFM, Leusbrock I, Grotenhuis JTC, Rijnaarts HNM (2013) Thermal performance and heat transport in aquifer thermal energy storage. Hydrogeol J.https://doi.org/10.1007/s10040-013-1066-0

Taku Ide S, Jessen K, Orr FM (2007) Storage of CO_2 in saline aquifers: effects of gravity, viscous, and capillary forces on amount and timing of trapping. Int J Greenh Gas Control 1(4):481–491. https://doi.org/10.1016/S1750-5836(07)00091-6

van der Schans ML, Bloemendal M, Robat N, Oosterhof A, Stuyfzand PJ, Hartog N (2022) Field testing of a novel drilling technique to expand well diameters at depth in unconsolidated formations. Groundwater 60(6):808–819. https://doi.org/10.1111/gwat.13203

van Lopik JH, Hartog N, Schotting RJ (2022) Using multiple partially-penetrating wells (MPPWs) to improve the performance of high-temperature ATES systems: well operation, storage conditions and aquifer heterogeneity. Geothermics 105:102537. https://doi.org/10.1016/j.geothermics.2022.102537

Vandenbohede A, Louwyck A, Vlamynck N (2014) SEAWAT-based simulation of axisymmetric heat transport. Groundwater 52(6):908–915. https://doi.org/10.1111/gwat.12137

Voss CI (1984) A finite-element simulation model for saturated-unsaturated, fluid-density-dependent groundwater flow with energy transport or chemically reactive single-species solute transport. US Geological Survey, Reston, VA

Ward JD, Simmons CT, Dillon PJ (2007) A theoretical analysis of mixed convection in aquifer storage and recovery: how important are density effects? J Hydrol 343(3–4):169–186. https://doi.org/10.1016/j.jhydrol.2007.06.011

Wenzlaff C, Winterleitner G, Schütz F (2019) Controlling parameters of a mono-well high-temperature aquifer thermal energy storage in porous media, northern Oman. Pet Geol 25(3):337–349. https://doi.org/10.1144/petgeo2018-104

Zheng C, Wang P (1999) MT3DMS v5.3: a amodular three-dimensional multispecies transport model for simulation of advection, dispersion and chemical reactions of contaminants in groundwater systems. Documentation and user's guide. https://erdc-library.erdc.dren.mil/jspui/handle/11681/4734. Accessed August 2026

Zuurbier KG, Zaadnoordijk WJ, Stuyfzand PJ (2014) How multiple partially penetrating wells improve the freshwater recovery of coastal aquifer storage and recovery (ASR) systems: a field and modeling study. J Hydrol 509(0):430–441. https://doi.org/10.1016/j.jhydrol.2013.11.057

Publisher's Note Springer Nature remains neutral with regard to jurisdictional claims in published maps and institutional affiliations.